*J. Fluid Mech.* (1992), *vol.* 244, *pp.* 339–376



# An experimental and numerical study of the Dean problem: flow development towards two-dimensional multiple solutions

By B. BARA,[1] K. NANDAKUMAR[2] AND J. H. MASLIYAH[2]

[1] Department of Mechanical Engineering, University of Alberta, Edmonton, Alberta, Canada T6G 2G8

[2] Department of Chemical Engineering, University of Alberta, Edmonton, Alberta, Canada T6G 2G6

(Received 16 August 1991 and in revised form 13 April 1992)

An experimental and numerical study investigating the flow development and fully developed flows of an incompressible Newtonian fluid in a curved duct of square cross section with a curvature ratio of 15.1 is presented. Numerical simulations of flow development from a specified inlet profile were performed using a parabolized form of the steady three-dimensional Navier–Stokes equations. No symmetry conditions were imposed. In general there was good agreement between the numerical predictions of the developing axial velocity profiles and LDV measurements. In addition, for computational expediency, the two-dimensional solution structure was calculated by imposing fully developed conditions together with symmetry conditions along the horizontal duct centreline.

Laser-Doppler measurements of axial velocity and flow visualization at Dean number $Dn = 125$, 137 and 150, revealed a steady and symmetric two-vortex flow at $Dn = 125$, and a steady and symmetric four-vortex flow at both $Dn = 137$ and 150 ($Dn = Re/(R/a)^{\frac{1}{2}}$, where $Re$ is the Reynolds number, $R$ is the radius of curvature of the duct and $a$ is the duct dimension). Axial velocity measurements showed that the four-vortex flow at $Dn = 150$ developed to the solution predicted by the two-dimensional numerical simulation. However, the four-vortex flow at $Dn = 137$ was still developing when the flow had reached the end of the 240° axial length of the duct. A numerical investigation for Dean numbers in the range of 50 to 175 revealed that at the limit point of the two-cell to four-cell transition the development length appeared to be infinite, and thereafter decreased for increasing Dean numbers. The behaviour of decreasing development length of the four-vortex flow with increasing Dean number has not been reported previously.

Using a symmetrically positioned pin at $\theta = 5°$ to induce the four-cell flows, the two-dimensional solution structure for $Dn \leqslant 150$ was experimentally observed for the first time. Experiments were consistent with the prediction by Winters (1987) that four-vortex flows are stable to symmetric perturbations, but unstable to asymmetric perturbations. Experimental and numerical investigations suggested that, when perturbed asymmetrically, the four-vortex flow might evolve to flows with sustained spatial oscillations farther downstream.

## 1. Introduction

The earliest observations of flow in curved pipes were by Williams, Hubbell & Finkell (1902) and Eustice (1910, 1911, 1925). Dean (1927, 1928*a*) was the first to

show mathematically the existence of one pair of counter-rotating vortices for the fully developed viscous flow of a Newtonian fluid in a curved pipe. Dean non-dimensionalized the equations of motion and found them to be characterized by a single non-dimensional parameter now known as the Dean number, $Dn$. Since Dean's original analysis, much work, both theoretical and experimental, has been done on flows in curved pipes. Apart from the hydrodynamic aspects, there has also been considerable work on forced-convection heat transfer in coiled pipes. The focus of this study was flow in a curved duct of square cross-section, so much of the past work in curved pipes has not been covered. The interested reader is directed to comprehensive review articles by Berger, Talbot & Yao (1983), Nandakumar & Masliyah (1986) and Itō (1987).

The first theoretical analysis showing the existence of secondary flows in a curved duct of rectangular cross-section was performed by Itō (1951) and Cuming (1952). Cheng & Akiyama (1970) used a finite-difference formulation to calculate the secondary flows in curved rectangular ducts. They calculated the familiar two-vortex pattern and only mentioned the existence of a new four-vortex pattern beyond a critical Dean number. The four-vortex pattern was later presented by Cheng, Lin & Ou (1975, 1976). A numerical investigation by Joseph, Smith & Alder (1975) for a curved duct of square cross-section also showed the switch from the twin counter-rotating vortices to the four-vortex pattern above a critical Dean number. They confirmed the presence of the four-vortex flow by flow visualization; however, no photographs were published. Photographs of the additional vortices, for square as well as other aspect-ratio cross-sections, have been presented by Cheng *et al.* (1979) and Sugiyama, Hayashi & Yamazaki (1983).

For flow in a curved duct, dual solutions were first reported in the numerical study by Cheng & Akiyama (1970) in their study of loosely coiled ducts of rectangular cross-section. Owing to uncertainties associated with the double solutions they did not present any results, but the double two- and four-vortex solutions were described in Akiyama (1969). The existence of dual solutions was established by Masliyah (1980), both numerically and experimentally, for the flow in a curved duct of semicircular cross-section with a flat outer wall. Dual solutions for fully developed flow in a curved duct of square cross-section have been found in the numerical studies of Winters & Brindley (1984), Shanthini & Nandakumar (1986), Winters (1987) and Daskopoulos & Lenhoff (1989). The study of Winters (1987) is the most detailed, showing the solution structure as a complex bifurcation diagram involving regions of multiple solutions consisting of symmetric and asymmetric solutions. A linear stability analysis by Winters revealed that the two-vortex flows were stable to an arbitrary perturbation, and the four-vortex flows were stable to a symmetric perturbation but unstable to an asymmetric perturbation. Despite their predicted instability, four-vortex flows have been visualized by Cheng *et al.* (1979) and Sugiyama *et al.* (1983) at certain Dean numbers in their experiments, but not as dual solutions (i.e. coexisting at the same Dean number as a two-vortex flow). Several features of Winters' (1987) solution structure are similar to the solution structures presented by Wienitschke, Nandakumar & Sankar (1990), Nandakumar, Raszillier & Durst (1991), and Nandakumar & Wienitschke (1991) for convective heat transfer in porous media, flow through rotating rectangular ducts, and mixed-convection heat transfer in a horizontal ducts respectively.

For fully developed flow in a curved pipe of circular cross-section, the numerical studies of Nandakumar & Masliyah (1982), Dennis & Ng (1982), and Yang & Keller (1986) revealed the existence of multiple solutions. Flow visualization by Masliyah

(1980) and Cheng & Yeun (1987) confirmed their existence in a curved pipe of semicircular and circular cross-section respectively. A stability analysis of the dual solutions, performed by Yanase, Goto & Yamamoto (1988), showed the two-vortex flow to be stable to an arbitrary perturbation, while the four-vortex flow was stable to a symmetric perturbation but unstable to an asymmetric perturbation.

Developing laminar flow in curved ducts of rectangular cross-section has been studied by Ghia & Sohkey (1977), Humphrey, Taylor and Whitelaw (1977), Yee, Chilukuri & Humphrey (1980), Taylor, Whitelaw & Yianneskis (1982), Hille, Vehrenkamp & Schulz-Dubois (1985), Sankar, Nandakumar & Masliyah (1988), Soh (1988), Sugiyama *et al.* (1989), Kajishima, Miyaki & Inaba (1989). The most detailed measurements of the flow development in a curved duct of square cross-section were performed in the LDV study by Hille *et al.* (1985). Their measurements revealed the development of an asymmetric four-vortex structure at Dean numbers between 150 and 300, but the flow had not reached a fully developed state within the 180° axial length of their duct. In the numerical study of the flow development in a curved duct of square cross-section, Sankar *et al.* (1988) found that is was possible for a four-vortex flow to develop sustained spatial oscillations in the streamwise direction. The numerical study by Soh (1988) showed that, depending on the inlet condition for a given flow rate, the flow might develop into the two-cell and four-cell states predicted by the two-dimensional bifurcation study of Winters (1987).

Most of the studies of flow development in a curved pipe have used a boundary-layer analysis to examine the details of the developing flow (see Yao & Berger 1988). Theoretical investigations in a curved pipe have only shown the development of a two-vortex flow, while the numerical studies in a rectangular geometry have shown the development of both a two- and four-vortex flow. For both a circular and rectangular cross-section, no experimental measurements exist for the development of a symmetric four-vortex flow to its fully developed state.

In this study, the existence of dual solutions in a curved duct of square cross-section was experimentally investigated. Detailed axial velocity measurements were performed to investigate the development of symmetric four-vortex flows. All experiments and numerical calculations were done for a curvature ratio of $R_c = 15.1$. Given that four-vortex flows have been calculated to be unstable to asymmetric perturbations, their stability characteristics were investigated in a combined numerical and experimental study.

## 2. Governing equations

A square-cross-section curved duct is best described by a cylindrical coordinate system as shown in figure 1. The origin of the coordinate system is at the centre of curvature of the duct, and the duct boundaries are located at $z' = \pm\frac{1}{2}a$ and $r' = R \pm \frac{1}{2}a$. By introducing the coordinate $x'$, where $x' = r' - R$, the side boundaries of the duct can more conveniently be located at $x' = \pm\frac{1}{2}a$.

In this study we wished to investigate the flow development and the flow structure once the flow had reached a fully developed state. Therefore, a numerical formulation of both the three-dimensional and two-dimensional Navier–Stokes equations were used in this study. The three-dimensional computer codes used in this study had been developed by Sankar *et al.* (1988), and the two-dimensional code had been developed by Shanthini (1985).

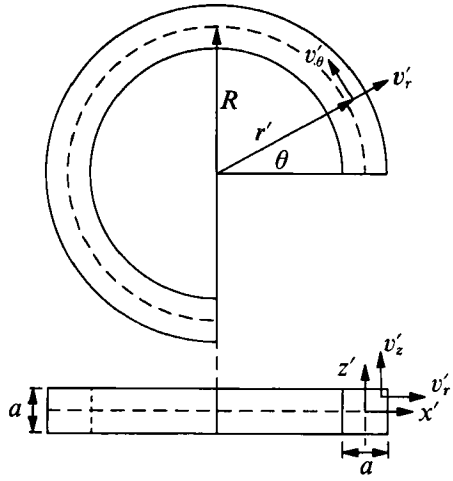


FIGURE 1. Cylindrical coordinate system.

### 2.1. *Developing flow equations*

The developing flow equations used in this study were simplified by neglecting the axial diffusion of momentum, changing the equations from an elliptic to a parabolic form. The non-dimensional continuity and parabolized momentum equations for a steady flow of an incompressible Newtonian fluid are

$$\frac{1}{r}\frac{\partial}{\partial r}(rv_r)+\frac{1}{r}\frac{\partial v_\theta}{\partial \theta}+\frac{\partial v_z}{\partial z}=0, \tag{2.1}$$

$$v_r\frac{\partial v_r}{\partial r}+\frac{v_\theta}{r}\frac{\partial v_r}{\partial \theta}-\frac{v_\theta^2}{r}+v_z\frac{\partial v_r}{\partial z}=-\frac{\partial p}{\partial r}+\frac{1}{Re}\left[\frac{\partial}{\partial r}\left(\frac{1}{r}\frac{\partial}{\partial r}(rv_r)\right)-\frac{2}{r^2}\frac{\partial v_\theta}{\partial \theta}+\frac{\partial^2 v_r}{\partial z^2}\right], \tag{2.2}$$

$$v_r\frac{\partial v_\theta}{\partial r}+\frac{v_\theta}{r}\frac{\partial v_\theta}{\partial \theta}+\frac{v_r v_\theta}{r}+v_z\frac{\partial v_\rho}{\partial z}=-\frac{1}{r}\frac{\partial p}{\partial \theta}+\frac{1}{Re}\left[\frac{\partial}{\partial r}\left(\frac{1}{r}\frac{\partial}{\partial r}(rv_\theta)\right)+\frac{2}{r^2}\frac{\partial v_r}{\partial \theta}+\frac{\partial^2 v_\theta}{\partial z^2}\right], \tag{2.3}$$

$$v_r\frac{\partial v_z}{\partial r}+\frac{v_\theta}{r}\frac{\partial v_z}{\partial \theta}+ +v_z\frac{\partial v_z}{\partial z}=-\frac{\partial p}{\partial z}+\frac{1}{Re}\left[\frac{1}{r}\frac{\partial}{\partial r}\left(r\frac{\partial v_z}{\partial r}\right)+\frac{\partial^2 v_z}{\partial z^2}\right], \tag{2.4}$$

Global continuity requires that

$$\int_{z=-0.5}^{z=0.5}\int_{r=R_c-0.5}^{r=R_c+0.5} v_\theta \,dr\,dz = 1.0. \tag{2.5}$$

The variables have been non-dimensionalized as follows:

$$r=\frac{r'}{a}=R_c+x,\quad x=\frac{x'}{a},\quad z=\frac{z'}{a},\quad R_c=\frac{R}{a},\quad v=\frac{v'}{\overline{v'_\theta}},\quad p=\frac{p'}{\rho\overline{v'_\theta}^2},\quad Re=\frac{\rho a\overline{v'_\theta}}{\mu},$$

where the prime denotes dimensional quantities. The above equations were solved using the computer code of Sankar *et al.* (1988). Their formulation did not impose any reflective symmetry about the $z'/a=0$ axis; therefore, it allowed the evolution of asymmetric flows in the $\theta$-direction. The equations were discretized by integrating them over a control volume and solved according to the method given by Patankar (1980). For all developing flow calculations, a grid of $31\times 31$ was used in the cross-

plane and a marching step of 0.5° was used in the axial direction. Typical computing times, in order to march 400° of axial length (i.e. 800 marching steps), were 1.2 hours of cpu usage on a FPS-164 Scientific Computer (Floating Point Systems Inc.).

The terms that were dropped from the full three-dimensional steady flow equations in Sankar *et al.*'s formulation were

$$\frac{1}{Re\,r^2}\frac{\partial^2 v_r}{\partial\theta^2}, \quad \frac{1}{Re\,r^2}\frac{\partial^2 v_z}{\partial\theta^2}, \quad \frac{1}{Re\,r^2}\frac{\partial^2 v_\theta}{\partial\theta^2}, \quad \frac{2}{Re\,r^2}\frac{\partial v_r}{\partial\theta}. \tag{2.6}$$

The terms are multiplied by $1/Re$ and $1/r^2$; therefore, in the absence of sharp velocity gradients, they will become less important as $Re$ and the radius of curvature increase. It is not shown in Sankar *et al.*, but on a careful examination of the details of their numerical formulation (Sankar *et al.* private communication), the gradient of $v_r$ in the $\theta$-direction was also neglected.

### 2.2. *Fully developed flow equations*

For the two-dimensional formulation of the Navier–Stokes equations, all the terms involving gradients in the axial direction, except for the axial pressure gradient, were dropped. As a result, the continuity and momentum equations for fully developed steady flow of an incompressible Newtonian fluid are

$$\frac{\partial v_r}{\partial r}+\frac{\partial v_z}{\partial z}+\frac{v_r}{r}=0, \tag{2.7}$$

$$v_r\frac{\partial v_r}{\partial r}+v_z\frac{\partial v_r}{\partial z}-\frac{v_\theta^2}{r}=-\frac{\partial p}{\partial r}+\frac{\partial}{\partial r}\left(\frac{1}{r}\frac{\partial}{\partial r}(rv_r)\right)+\frac{\partial^2 v_r}{\partial z^2}, \tag{2.8}$$

$$v_r\frac{\partial v_\theta}{\partial r}+v_z\frac{\partial v_\theta}{\partial z}+\frac{v_r v_\theta}{r}=-\frac{1}{r}\frac{\partial p}{\partial\theta}+\frac{\partial}{\partial r}\left(\frac{1}{r}\frac{\partial}{\partial r}(rv_\theta)\right)+\frac{\partial^2 v_\theta}{\partial z^2}, \tag{2.9}$$

$$v_r\frac{\partial v_z}{\partial r}+v_z\frac{\partial v_z}{\partial z}=-\frac{\partial p}{\partial z}+\frac{1}{r}\frac{\partial}{\partial r}\left(r\frac{\partial v_z}{\partial r}\right)+\frac{\partial^2 v_z}{\partial z^2}. \tag{2.10}$$

The equations have been non-dimensionalized as follows

$$p=\frac{a^2\rho p'}{\mu^2}, \quad v_r=\frac{a\rho v_r'}{\mu}, \quad v_\theta=\frac{a\rho v_\theta'}{\mu}, \quad v_z=\frac{a\rho v_z'}{\mu},$$

with $r$, $x$, $z$ and $R_c$ scaled as for the developing flow. The different scaling for $p$ and $v$ as compared to the developing flow equations is to allow the two-dimensional equations to be solved without involving iteration of the axial pressure gradient.

Equations (2.7)–(2.10) can be transformed to a vorticity–stream-function formulation by introducing a dimensionless stream function and vorticity function. The dimensionless stream function which automatically satisfies continuity is determined by

$$v_r=\frac{1}{r}\frac{\partial\psi}{\partial z}, \quad v_z=-\frac{1}{r}\frac{\partial\psi}{\partial r}; \tag{2.11}$$

the dimensionless vorticity function is defined as

$$\Omega=\frac{\partial v_z}{\partial r}-\frac{\partial v_r}{\partial z}. \tag{2.12}$$

Substituting (2.11) into (2.12) results in the vorticity–stream-function equation

$$\frac{\partial^2\psi}{\partial r^2}+\frac{\partial^2\psi}{\partial z^2}-\frac{1}{r}\frac{\partial\psi}{\partial r}=-r\Omega. \tag{2.13}$$

Using (2.12), the radial and vertical momentum equations can be combined to eliminate the pressure terms and form the vorticity-transport equation

$$v_r\frac{\partial\Omega}{\partial r}+v_z\frac{\partial\Omega}{\partial z}-\frac{v_r\Omega}{r}=\frac{-2v_\theta}{r}\frac{\partial v_\theta}{\partial z}+\frac{\partial^2\Omega}{\partial r^2}+\frac{\partial^2\Omega}{\partial z^2}+\frac{1}{r}\frac{\partial\Omega}{\partial r}-\frac{\Omega}{r^2}. \tag{2.14}$$

The axial momentum equation remains

$$v_r\frac{\partial v_\theta}{\partial r}+v_z\frac{\partial v_\theta}{\partial z}+\frac{v_rv_\theta}{r}=-\frac{1}{r}\frac{\partial p}{\partial\theta}+\frac{\partial^2v_\theta}{\partial r^2}+\frac{\partial^2v_\theta}{\partial z^2}+\frac{1}{r}\frac{\partial v_\theta}{\partial r}-\frac{v_\theta}{r^2}. \tag{2.15}$$

The solution to the two-dimensional flow field can now be found by solving (2.13), (2.14) and (2.15).

For a square duct, the boundary conditions with imposed symmetry about the horizontal centreline are:

no slip at the walls $\psi=v_r=v_\theta=v_z=0,$

at the top wall $\Omega=-\frac{1}{r}\frac{\partial^2\psi}{\partial z^2},$

at the sidewalls $\Omega=-\frac{1}{r}\frac{\partial^2\psi}{\partial r^2},$

along the horizontal centre line

$$\psi=\Omega=\frac{\partial v_\theta}{\partial z}=\frac{\partial v_r}{\partial z}=v_z=0.$$

The equations were solved using the computer programs written by Shanthini (1985). In her formulation (2.13), (2.14) and (2.15) were discretized using a three-point central-difference approximation. The imposed symmetry about $z'/a=0$ did not allow any asymmetric solutions to be calculated. A grid of $41\times21$ was used in all of the two-dimensional calculations performed in this study. Typical computing times for one two-dimensional simulation were four to five minutes of cpu usage on the FPS-164 Scientific Computer.

### 2.3. *Definition of Dean number*

Even though the governing equations are not characterized by a single non-dimensional parameter, it is common practice to present results characterized by a non-dimensional Dean number. The Dean number, $Dn$, used throughout this study, was defined as

$$Dn=Re/R_c^{\frac{1}{2}}, \tag{2.16}$$

where $Re=\rho a\overline{v_\theta'}/\mu$ and $\rho$ is the fluid density and $\mu$ is the absolute viscosity. The Dean number is similar to Dean's (1928*a*) non-dimensional grouping which included a curvature ratio and a slightly different form of Reynolds number. The Dean number is a ratio of the inertial and centrifugal forces to the viscous forces. Secondary flows are a result of the interaction of the centrifugal forces with the

viscous forces, so the Dean number is a measure of the strength of the secondary flow. Many definitions of Dean number have been used in the analysis of curved ducts and a review is given by Berger *et al.* (1983).

## 3. Experimental system

A schematic of the curved duct apparatus is shown in figure 2. The curved duct section had a 1.27 cm square cross-section with an axial length of 270° and a curvature ratio $R_c = 15.1$. The square duct was constructed by first cutting a square channel into the edge of 19.8 cm diameter, 3.3 cm thick Plexiglas disk. A strip of 1.5 mm thick Plexiglas was then glued around the edge of the disk to form the outer wall. A stilling chamber, with a smooth contraction connected to a 1 m straight duct inlet section, was used to provide a well-controlled inlet profile to the curved section. A 10 cm long by 1.9 cm diameter straight pipe was fastened directly to the exit of the curved section. A tee connection fastened to the end of the straight pipe was fitted with a flexible tubing coupling and an air bleed valve. At 5° from the curved section inlet, a hole was drilled along a radial line through the outer wall at $z' = 0$ to allow a 0.4 mm diameter pin to be inserted across the duct, which would allow the introduction of symmetric and asymmetric perturbations into the flow.

The curved section, inlet section and stilling chamber were all made of Plexiglas to facilitate LDV measurements and flow visualization. The assembly was mounted on a platform that allowed rotation about the centre of the curved section and the ability to traverse vertically and horizontally. Owing to physical limits in the amount that the assembly could be rotated, only about 240° of axial length was accessible for measurement purposes. Traversing of the apparatus was necessary because the LDV optics were held stationary; however, this resulted in an uncertainty of $\pm 2$–3 % in positioning the crossing point in the duct.

In order to provide a steady flow rate, a constant-head system consisting of stainless steel overflow tanks positioned above and below the apparatus was used. The distance between water levels in the two overflow tanks was approximately 3.5 m, with the apparatus being about 0.5 m higher than the lower tank. The bottom of each overflow tank was lined with a 7.5 cm thick piece of foam in order to damp fluctuations caused by fluid entering the tanks. A reservoir with a centrifugal pump supplied the upper overflow tank, while the lower overflow tank would return to the reservoir or drain depending on if the system was run as a closed or opened loop. Two bleed valves, one located on the stilling chamber and the other at the exit of the curved section, were installed to allow air to be purged from the system. A set point temperature controller was used to keep the working fluid to within $\pm 0.1$ °C when measuring velocities in the closed system, or injecting dye in the open system configuration.

A rotameter was used to aid in the setting of a desired flow rate but the mass flow rate was determined by weighing the amount of water collected in a timed interval. Timing was done with a hand-held digital stop watch with a resolution of 0.01 s, and the sample was weighed on an electronic balance accurate to 0.1 g. Uncertainty in an experimentally determined Dean number was $\pm 0.3$ %.

The inlet section of the curved duct apparatus consisted of the stilling chamber and the 1 m long straight section. Careful attention was paid to the design of these two components to ensure that a well-behaved flow was present at the inlet of the curved section. One major aspect of this study was to investigate the effect of perturbations on the curved duct flow, so a stable and clean inlet condition was

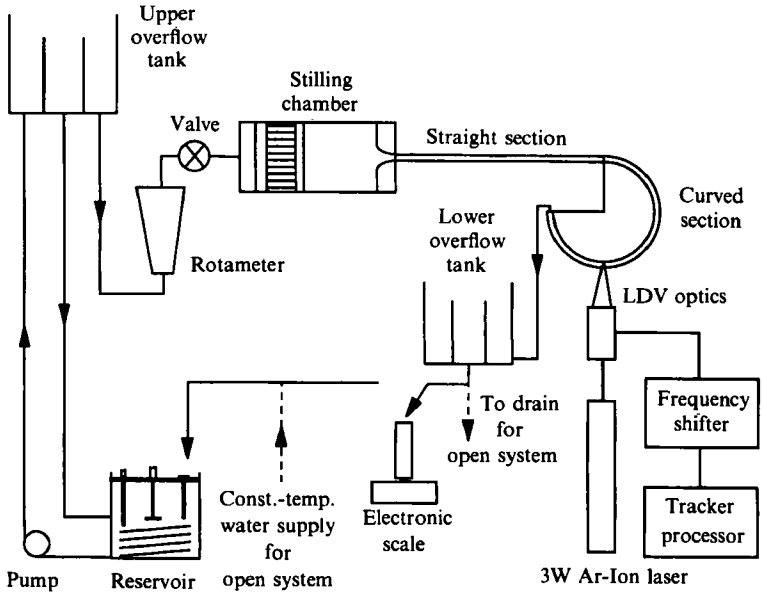


FIGURE 2. Schematic of curved duct apparatus.

absolutely necessary. A fully developed straight duct flow was chosen to be the inlet profile to the curved section. A 1 m straight section was used, based on the measurements of Goldstein & Kreid (1967). Using their experimentally determined relation $L/d_h = 0.09Re$, where $L$ is the development length and $d_h$ is the hydraulic diameter, a 1 m length of duct would provide a fully developed inlet profile up to a Dean number of $Dn = 225$.

In order to ensure that the profile would develop properly in the straight duct, a stilling chamber with a flow straightener, screens and contraction was used to feed the straight section. Details of the stilling chamber design can be found in Bara (1991). The four curved surfaces of the contraction were quarter-ellipses with minor and major axes of 2.5 cm and 5.0 cm respectively. This resulted in a contraction with a contraction ratio, based on area, of 25 to 1. The quarter-ellipse, based on the experimental system of Beavers, Sparrow & Magnuson (1970), was chosen to provide a uniform entry profile to the straight section.

Axial velocities were measured with a single-component Argon-ion laser-Doppler velocimeter (LDV) operating in backscatter mode with a frequency tracker performing the signal processing. The system was composed of Dantec 55X modular optics with a 80 mm focal length front lens, a Bragg cell and a Dantec 55N10 Frequency Shifter. A Coherent Innova 90-3 Argon-ion laser capable of 3 W output on all lines was used as the lasing source. All velocity measurements were made using the blue (488.0 nm) line with typical laser powers of 200 mW. Measurements were performed by passing the laser beams through the 1.5 mm thick outer wall of the curved duct. The flow was seeded with silicon carbide particles of mean diameter $1.5 \times 10^{-6}$ m.

The probe volume, formed by the crossing point of the laser beams, is an ellipsoid with the axis in the direction of the beams much elongated. For the optical arrangement used in this study the probe volume had a diameter of 0.017 mm and a length of 0.12 mm. With a duct dimension of 1.27 cm this gave about 100 resolvable points across the duct. Uncertainty in a velocity measurement was about $\pm 0.3\%$,

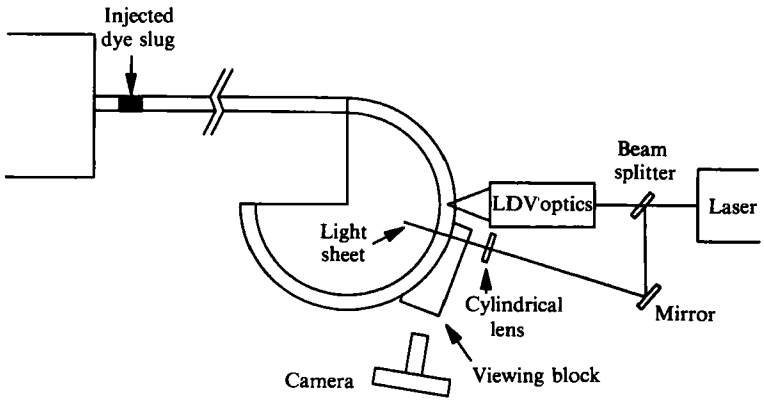


FIGURE 3. Schematic of flow visualization system.

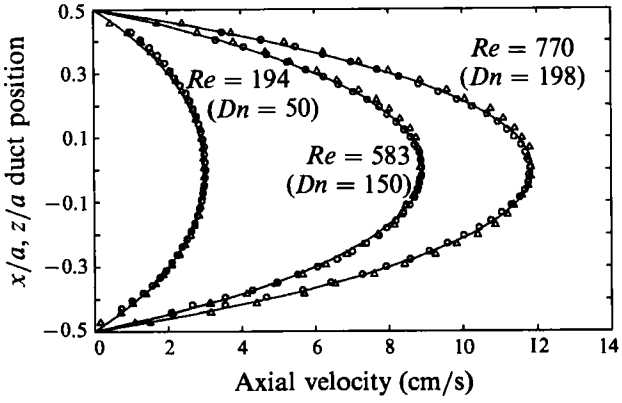


FIGURE 4. Comparison of measured inlet velocity profiles (○, $z'/a = 0$; △, $x'/a = 0$) to analytical predictions (——) (measurement location: 5 hydraulic diameters upstream of inlet).

while uncertainty in a non-dimensional velocity, $v_\theta$, was $\pm 0.45\%$. The largest source of error in the velocity measurements was not the uncertainty in the measurement itself, but the $\pm 2$–$3\%$ uncertainty in positioning the crossing point in the duct.

### 3.1. *Flow visualization*

Flow visualization was accomplished by illuminating a cross-plane of the square duct with a thin sheet of blue laser light and injecting a laser fluorescent dye into the flow. A schematic of the flow visualization system is shown in figure 3. Dye was injected through a 0.4 mm diameter hole drilled through the top wall of the straight section duct at 9.3 cm from the end which was connected to the stilling chamber. As the dye passed through the plane illuminated by the laser light its fluorescence was bright enough to allow photographs to be taken. The image was viewed through a moveable Plexiglas block with flat outer edges. A thin film of water between the viewing block and outer wall of the duct was necessary to allowing viewing of the image. Rhodamine 6G (also known as Rhodamine 590) at a concentration of $1 \times 10^{-3}$ M was used as the dye source. Rhodamine B and Fluorescein at similar molar concentrations were also tried but did not give as bright an illumination as the Rhodamine 6G.

Flow patterns were photographed with a 35 mm Nikon SLR camera fitted with a 105 mm Nikon lens and a Nikon TC-200 2 × teleconverter. A No. 12 Kodak Wratten

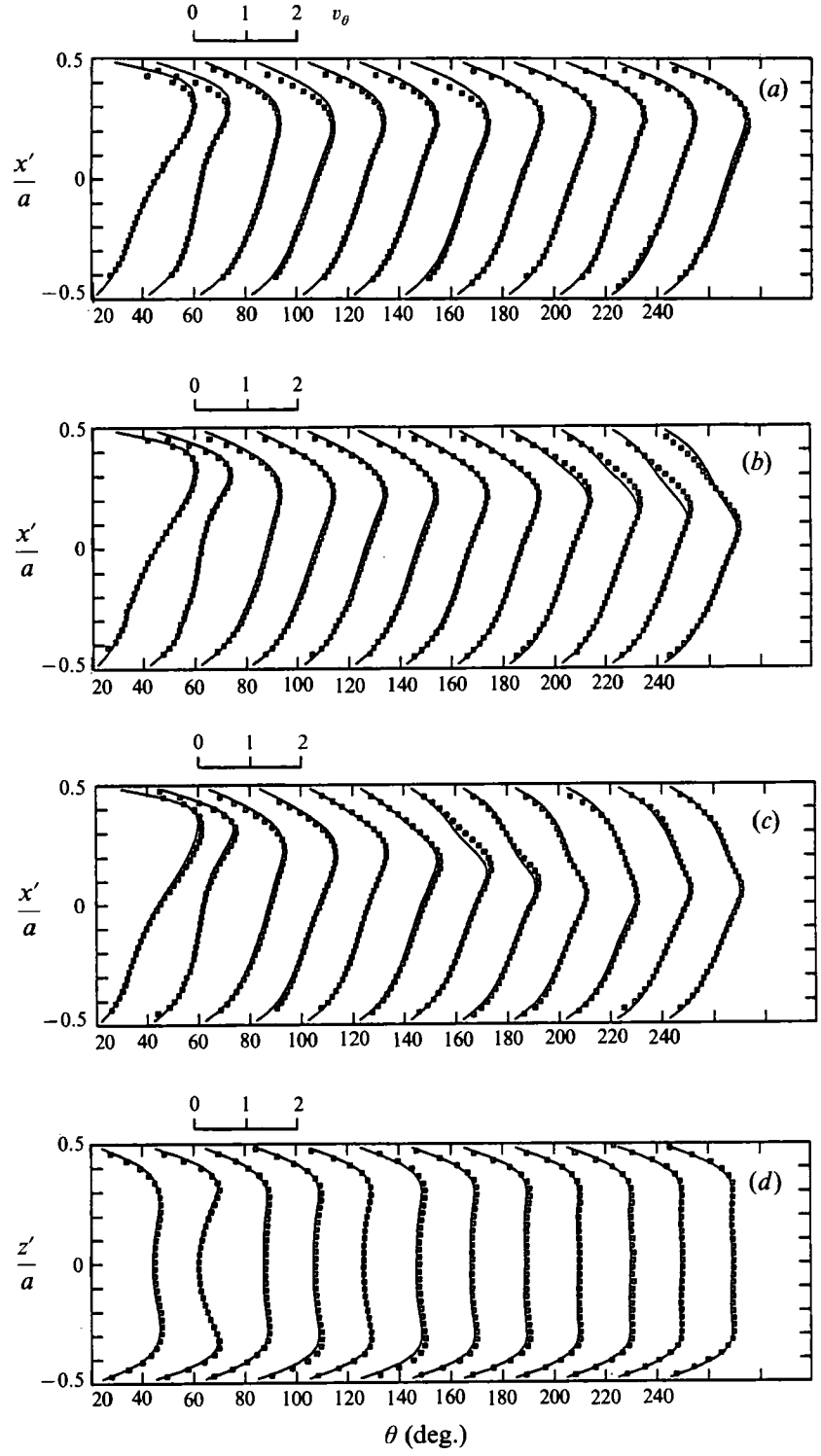


FIGURE 5. Measured axial velocity profiles (□) compared to three-dimensional numerical simulations (——) at (*a*) $Dn = 125$, (*b*) 137 and (*c*) 150. Horizontal profiles in (*a–c*) are at $z'/a' = 0$. (*d*) Vertical profiles at $x'/a = 0$ at $Dn = 150$.

Gelatin filter was attached to the lens assembly to attenuate the blue light of the illuminating sheet but still allow the light from the fluorescing dye to pass through. Good separation of the two colours was achieved since the peak fluorescence of the dye was around 580–600 nm (Yarborough 1974), while the illuminating sheet was at 488 nm. Typical exposure times were from $\frac{1}{30}$ to $\frac{1}{100}$ s with a lens aperture of $f4$ and ISO (ASA) setting of 800. P800/1600 Kodak Ektachrome professional slide film was used because of its fast speed and fine grain size. When taking photographs, stray reflections were minimized by covering the curved section with black felt.

Digital enhancement of the photographed flow patterns was required to trim off unwanted reflections and linearly stretch the photographs in the radial direction. The different refractive indexes between water and air, and the refraction of light at the curved surface interface between the viewing block and duct, caused the viewed image to be compressed in the radial direction. Reflections of the illuminated flow patterns appeared around the duct boundary, but had no adverse effect on viewing the desired image. Photographs were digitized with the assistance and equipment of Campbell (1991). The technique consisted of illuminating the image of the flow patterns contained on a slide, and then capturing the image digitally with a Hitachi VKC360 video camera connected to a Data Translation 2871 digital frame grabbing board. The resulting digital images of the flow patterns had a resolution of 512 pixels in the vertical direction and 480 pixels in the radial direction.

## 4. Flow development towards fully developed symmetric flows

### 4.1. *Inlet flow*

The inlet condition to the curved section that was used in this study was a fully developed laminar straight duct flow. Figure 4 shows the analytically predicted profiles (from Shah & London 1978) compared to the velocity profiles that were measured at 5 hydraulic diameters upstream of the curved section inlet. Horizontal and vertical axial velocity profiles were measured at the horizontal and vertical duct centrelines respectively. The measured data are in very good agreement with the analytical prediction, confirming that, for the range of Reynolds numbers investigated, the measured velocity profile had reached the fully developed state.

In the numerical simulations of developing flow, the inlet profile was calculated using a simple approximation (from Shah & London 1978) for the analytical solution. The simple approximation predicts values that are higher than the analytical solution in the central region of the duct. The maximum non-dimensional velocity predicted by the analytical solution at $x'/a = z'/a = 0$ is 2.096, while the simple approximation predicts a value of 2.116 at the same location. The difference is only 1%, so the simple approximation is a good estimate of the analytical solution.

### 4.2. *Flow development*

In order to investigate the flow development, flow visualization and axial velocity measurements were performed at three Dean numbers, $Dn = 125$, 137 and 150. Starting at an axial position of 20°, axial velocity profiles were measured every 20° up to an axial position of 240°. Photographs were taken at each location to visualize the development of the secondary flows. Using the parabolized formulation of the three-dimensional Navier–Stokes equations, numerical simulations of the flow development corresponding to the measurements were performed.

The development of axial velocity profiles with downstream position at $Dn = 125$, 137 and 150 is shown in figure 5 (*a–c*). The outer wall of the duct is at $x'/a = 0.5$. For

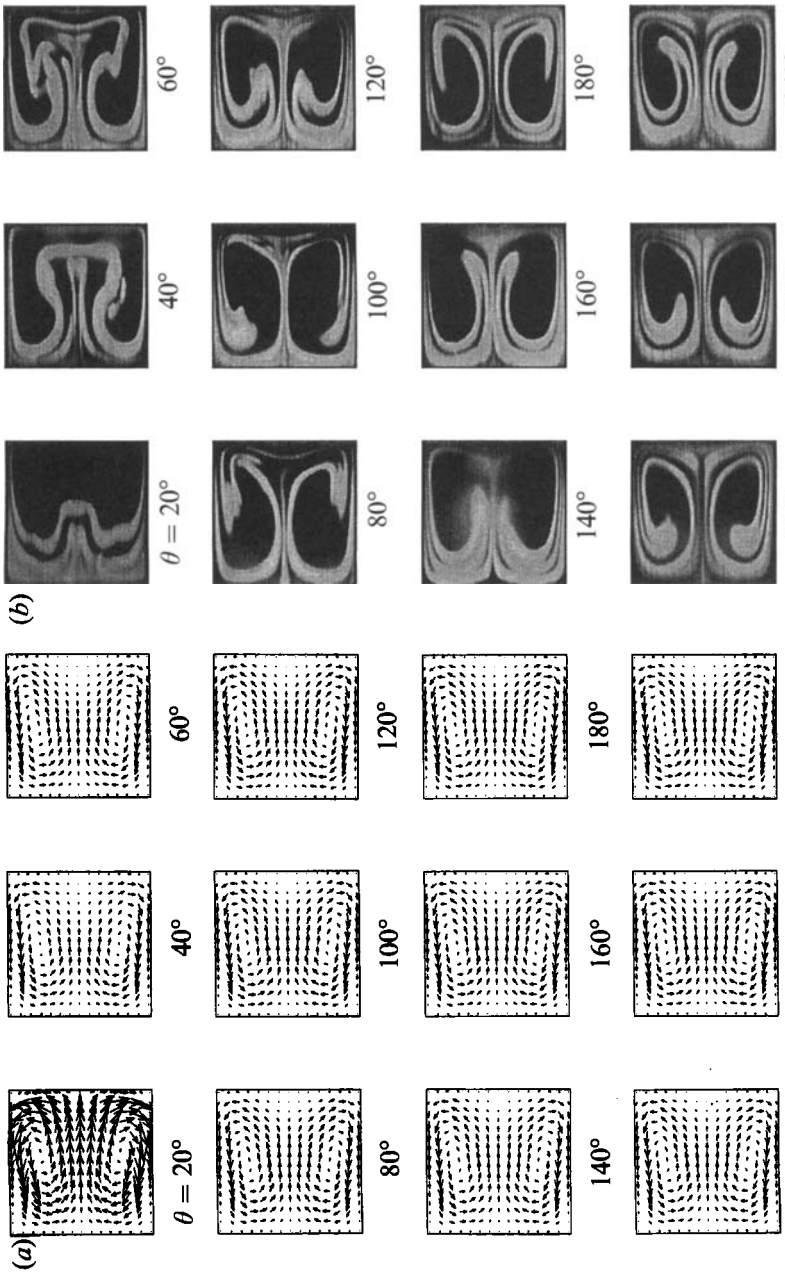


FIGURE 6. (*a*) Arrow plots showing secondary flow development every 20° at $Dn = 125$. (*b*) Flow visualization showing secondary flow development every 20° at $Dn = 125.5$.

each downstream position, the measured horizontal axial velocity profile at the horizontal duct centreline (i.e. $z'/a = 0$) is compared to the numerically predicted profile. Vertical axial velocity profiles, measured at $Dn = 150$ and the vertical centreline of the duct (i.e. $x'/a = 0$) are compared to numerical predictions in figure 5(*d*). The numerical prediction of secondary flow development for each Dean number is presented in figures 6(*a*) 7(*a*) and 8(*a*) in the form of arrow plots showing the secondary velocity vectors. All secondary velocities have been normalized with the mean axial velocity to show the relative strength of the secondary flow with downstream position. The outer wall is on the right-hand side of each arrow plot, and the length of the mean axial velocity vector is equal to the length of the duct walls. Flow visualization of the development of the secondary flow patterns for each Dean number is shown in figures 6(*b*), 7(*b*) and 8(*b*). Again the outer wall is on the right-hand side.

### 4.2.1. *Flow development at* $Dn = 125$

The development of the axial velocity profiles shown in figure 5(*a*) is similar to the observations of Austin & Seader (1974) for flow in a curved pipe, and Hille *et al.* (1985) for flow in a curved duct of square cross-section. The profiles exhibit the characteristic initial transfer of momentum to the outer wall, with a back-transfer of momentum as the secondary flow becomes developed. The overall agreement with the numerical predictions is good, indicating that the parabolic assumption is valid at this Dean number. A slight increase in the axial velocity near the central region of the duct at 240° suggests that some exit effect might have been present.

In the fully developed region, which occurred after an axial position of about 100°, it can be seen that the measured velocities are slightly in error. The error appears to be systematic in nature, causing the measured values to be generally higher than the predictions. The magnitude of the velocity errors in the central region of the duct are between 2% and 3%. Given that the uncertainty in $v_\theta$ was $\pm 0.45\%$, the errors were obviously caused by positioning errors in the duct. The consistently lower values of the measurements near the outer wall are likely to be due to the tendency of the tracker processor to measure low in this region.

As the flow initially developed, the fully developed straight duct inlet profile, with its velocity maximum at the duct centre, was quickly skewed toward the outer wall. This large transfer of axial momentum is seen at 20° in figure 5(*a*), where the axial velocity maximum has been shifted toward the outer wall. This initial transfer of momentum is a result of the fluid in the straight duct flowing toward the outer wall of the curved section which is in line with the straight duct axis. Examining the secondary velocity arrow plot at 20° in figure 6(*a*), it can be seen that a strong secondary flow toward the outer wall is present, and a return flow at the top and bottom walls of the duct has been established. The return flow has been set up in response to favourable pressure gradient caused by the high-pressure region at the outer wall. The maximum flow velocity toward the outer wall is 16% of the mean, while the maximum velocity in the region returning fluid toward the inner wall is 22.5% of the mean.

At 40° from the inlet, the peak in the axial velocity profile has decreased and started to move back toward the duct centre. In addition, the axial velocity near the inner wall has increased. This redistribution of axial momentum is a result of the secondary flow transporting the high-momentum fluid at the outer wall to the inner wall. From the arrow plot at 40°, it can be seen that the strength of the secondary flow toward the outer wall has decreased, as the initial linear momentum of the straight duct flow has been dissipated. The maximum secondary velocity directed

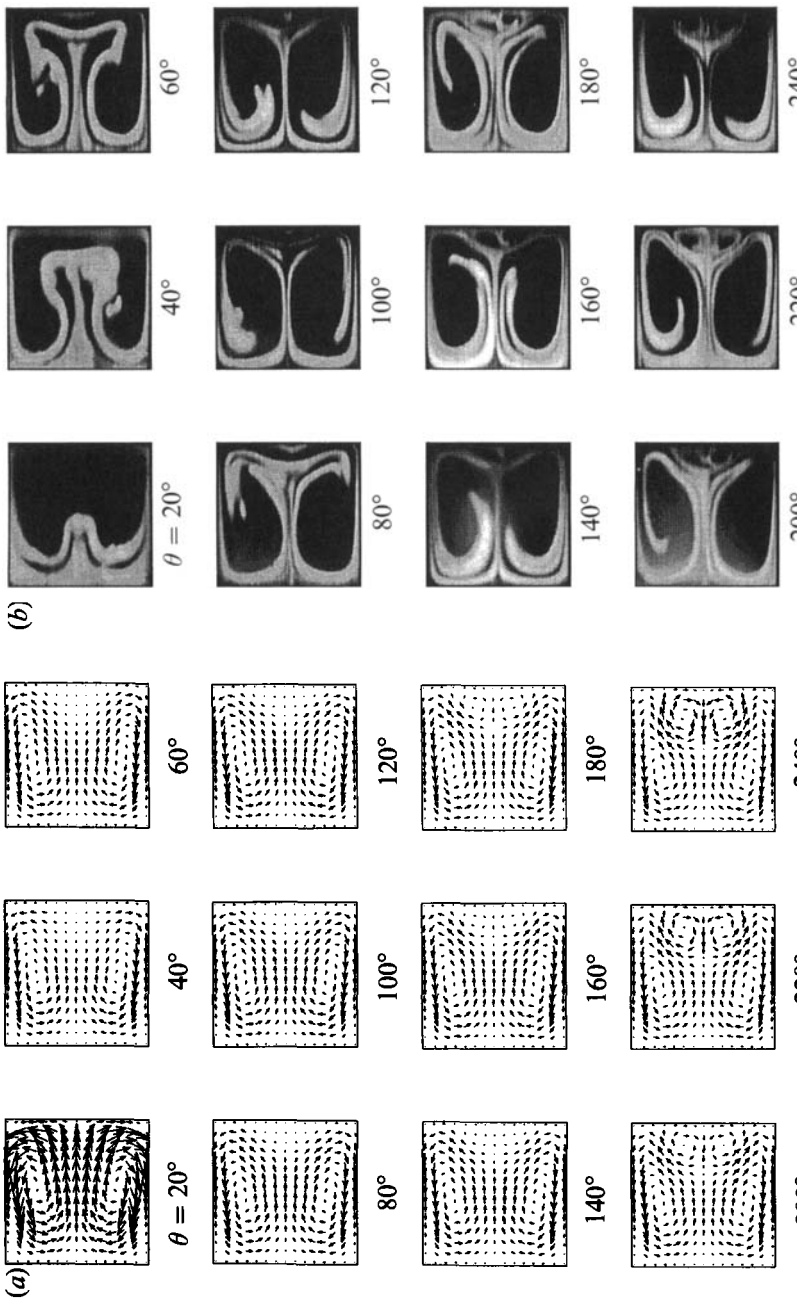


FIGURE 7. (*a*) Arrow plots showing secondary flow development every 20° at $Dn = 137$. (*b*) Flow visualization showing secondary flow development every 20° at $Dn = 137.1$.

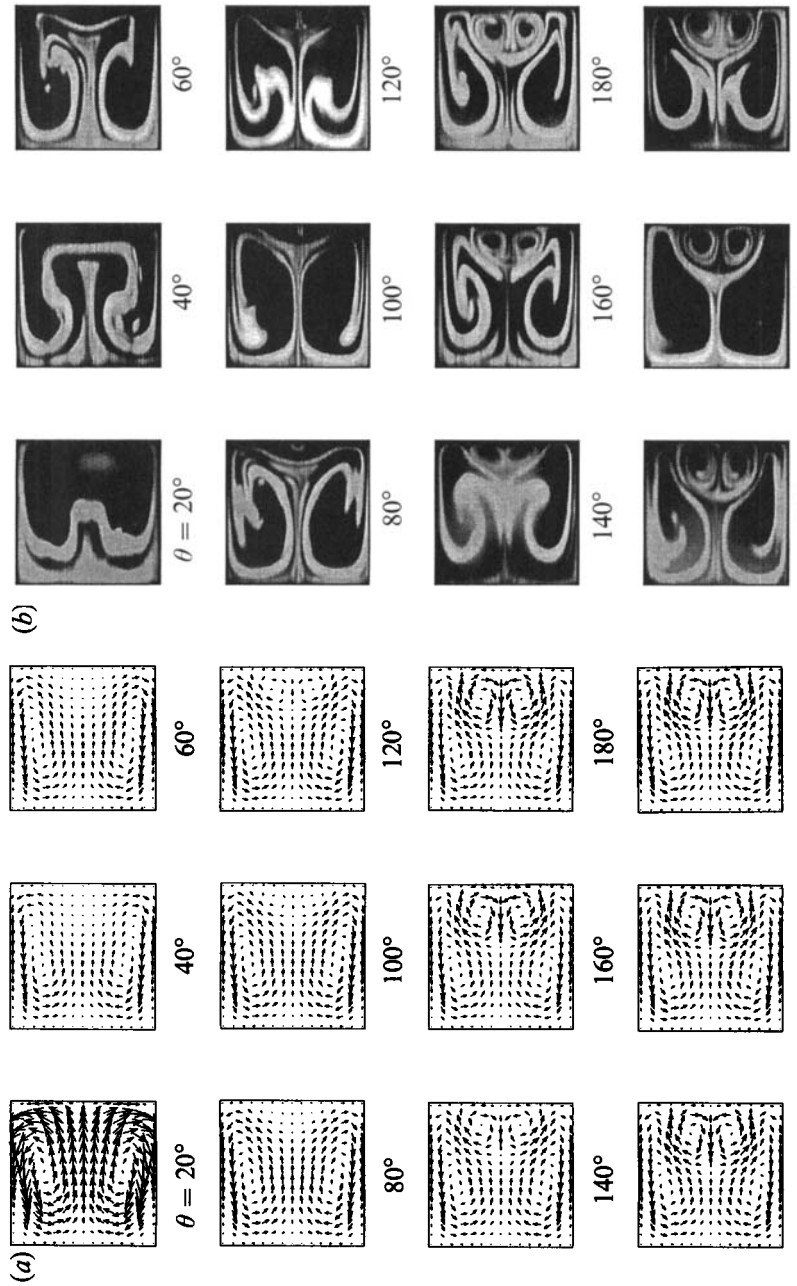


FIGURE 8. (*a*) Arrow plots showing secondary flow development every 20° at $Dn = 150$. (*b*) Flow visualization showing secondary flow development every 20° at $Dn = 149.9$.

toward the outer wall on the duct centreline is 5.3% of the mean, while the inward flow at the top and bottom walls has a maximum secondary velocity of 12.5% of the mean.

At 60° from the inlet, some further transfer of axial momentum from the outer wall toward the duct centre has occurred, filling in the central region of the profile. The maximum secondary velocities have not significantly changed from the values at 40°, as is evident in the arrow plot at 60°. At 80° there is a slight decrease in the axial momentum in the central region of the duct, but no more appreciable changes occur at 100°. After 80° the secondary velocities settle down to maximum values of 6.2% and 12.9% of the mean in the outward and inward flows respectively. Judging from the axial velocity measurements and the arrow plots of the secondary flow, it can be concluded that after 100° the flow has become fully developed.

Flow visualization in figure 6(*b*) shows that symmetry about the horizontal duct centre-line was retained throughout the entire development process. Flow visualization is useful in showing the boundaries of the cells, but no velocity information can be obtained. The cell boundaries are traced out by the dye as the secondary flow carries the fluid around the cross-section. Given the ratio of the mean axial velocity to the secondary velocities, a fluid particle will on average rotate once around the top or bottom half of the duct approximately every 70° to 80° of axial length. This effect is evident in the flow visualization at 20° and 40°, since the dye has not yet completed one revolution in the cross-section.

In the studies of Austin & Seader (1974) and Humphrey *et al.* (1977), double peaks in the axial velocity profiles were observed in the development of axial velocity. This was not observed in this study because the curvature of the duct was not strong enough. In strongly curved ducts, more axial momentum is initially transferred toward the outer wall than in gently curved ducts, so the secondary flow will bring fluid with higher momentum to the inner wall. This causes the slow moving fluid at the inner wall to be displaced toward the duct centre leaving high-momentum fluid at the inner wall, thus creating the double peak. Maximum secondary velocities of 23% of the mean in this study as compared to 65% of the mean in the study of Humphrey *et al.* (1977) shows the effect that stronger curvature has in increasing the strength of the secondary flow.

### 4.2.2. *Flow development at* $Dn = 137$

The initial development of the axial velocity profiles at $Dn = 137$, shown in figure 5(*b*), is very similar to the developmental at $Dn = 125$. Up to $\theta = 80°$ the axial velocity profiles for the two Dean numbers are almost identical. Flow visualization and arrow plots up to $\theta = 80°$ are also very similar for the two cases. The numerical predictions of the secondary flows revealed that the maximum secondary velocities, on average, differed by about 0.5% in this initial development region. These observations show that the initial flow development at $Dn = 137$ is to a two-vortex structure.

After $\theta = 80°$ the flow development at $Dn = 137$ starts to differ from the development observed at $Dn = 125$. At $Dn = 125$ the axial velocity profile was fairly well established by $\theta = 80°$, with no further changes observed with axial position. However, the axial velocity profile at $Dn = 137$ and $\theta = 100°$ is starting to show a slight shift of the maximum axial velocity back toward the duct centre. Examining the flow visualization at $\theta = 100°$ in figure 7(*b*), it is seen that an additional pair of vortices are starting to form at the outer wall. In response to the additional vortices, the peak in the axial velocity profile is starting to shift back toward the duct centre.

The magnitudes of the secondary flows at the outer wall are very small, as is evident from the arrow plot.

The flow visualization in figure 7(*b*) shows that the additional vortices continue to grow with downstream distance and are still growing at 240°, indicating that the flow has not reached a fully developed state. The numerical prediction of secondary velocities indicate that slightly over 300° of development length are required before the maximum radial velocities settle down to constant values. Once the secondary velocities have reached a constant value, the maximum radial velocity that occur on the horizontal duct centreline in the additional vortex pair is about 10% of the mean axial velocity. The maximum secondary velocity in the larger vortex pair is about 11.5% of the mean. As for $Dn = 125$, this occurs near the top and bottom walls in the flow returning fluid to the inner wall.

The response of the axial velocity profiles to the increasing size and strength of the additional vortex pair is an increasing shift of the maximum velocity back toward the duct centre. With the opposite sense of rotation as compared to the large vortices, the second vortex pair is able to transfer high-momentum fluid toward the duct centre and cause the velocity maximum to shift. Comparing the measured velocity profiles to the numerical simulations at $\theta = 180°$, 200° and 220°, it can be seen that the numerical simulation predicts a faster growth rate of the additional vortices than observed. The larger vortex strength predicted by the simulation causes a larger shift in the maximum of the axial velocity. This is evident from the difference between the measurements and the numerical predictions near the outer wall. The difference at each location (i.e. $\theta = 180°$, 200° and 220) is larger than the 2–3% positioning error, so it is clearly due to the different growth rates of the additional vortex pair. The faster growth rate of the additional vortices is also evident by comparing the arrow plots with the flow visualization. The reason why the simulation differs from the experiments is because the numerical formulation neglects elliptic effects in the axial direction and ignores gradients of the radial velocity in the axial direction.

The flow visualization in figure 7(*b*) shows that the additional vortices retained their symmetry about the horizontal centreline throughout the investigated development length, contrary to the asymmetric development that was observed by Hille *et al.* (1985). This difference might be due to the stronger curvature of their duct or possible physical asymmetries in their apparatus, given that the four-vortex solutions are unstable to asymmetric perturbations. However, the existence of their additional pair was first observed after $\theta = 108°$, in qualitative agreement with the present study.

#### 4.2.3. *Flow development at* $Dn = 150$

As seen in figure 5(*c*), the flow development up to $\theta = 60°$ is essentially the same at $Dn = 150$ as it was for $Dn = 137$ and 125, as indicated by the axial velocity profiles, arrow plots and flow visualization. At $\theta = 20°$, the predicted maximum secondary velocity at the top and bottom walls was 24.8% of the mean, as compared to 23.7% and 22.5% for $Dn = 137$ and 125 respectively. The slight increase in the secondary flow velocity is a direct result of the increased centrifugal force at the higher Dean numbers. It is not surprising that the initial flow development is similar, given that for each case the secondary flow is induced in response to the pressure gradient set up by the fluid moving toward the outer wall. At $\theta = 80°$ the flow visualization in figure 8(*b*) suggests that an additional pair of vortices is starting to form at the outer wall. Similar to the flow development at $Dn = 137$, the axial velocity profile at $Dn = 150$ and $\theta = 80°$ is starting to show the back-transfer of momentum toward the

duct centre in response to the appearance of the additional vortices. The appearance of the additional vortices occurs at an earlier downstream position for $Dn = 150$ than for $Dn = 137$. From the flow visualization sequence, it is seen that the additional vortices continue to grow in the downstream direction, but at a faster rate than at $Dn = 137$.

Comparing the horizontal axial velocity profiles at $\theta = 140°$ and $\theta = 160°$ to the numerical simulation, it can be seen that the numerical simulation predicts a slightly faster growth rate of the additional vortices. This is evident by the larger shift in the axial velocity profiles toward the duct centre for the numerical simulations. As for $Dn = 137$, the observed difference is not due to experimental uncertainty in the measured velocities.

Comparison of the arrow plots and flow visualization at $\theta = 140°$ and $160°$ shows the larger vortices predicted by the numerical simulation. From $\theta = 180°$ to $240°$, the measured axial velocity profiles and flow visualization are in good agreement with the numerical simulation. Both measurements and numerical predictions indicate that by $\theta = 240°$ the flow has reached a fully developed state. Once the secondary velocities have reached a constant value, the maximum radial velocity that occurs on the horizontal duct centreline in the additional vortex pair is about 11% of the mean axial velocity. This is slightly larger than the maximum value of 10% at $Dn = 137$. For both $Dn = 150$ and 137, the maximum secondary velocity in the larger vortex pair is about 11.6% of the mean axial velocity.

The measured vertical profiles of axial velocity in figure 5(*d*), and the flow visualization in figure 8(*b*) reveal that the flow development was symmetric about the horizontal duct centreline. The measured vertical profiles are in good agreement with the numerical predictions. The large dip in the vertical axial velocity profile at $\theta = 40°$ is a result of the secondary flow redistributing the axial momentum in the initial development region. This dip in the vertical profile was also observed by Austin & Seader (1974) for developing flow in a curved pipe. The onset of the additional pair of vortices at $Dn = 150$ and 137 is consistent with the instability explanation given by Cheng *et al.* (1976), who believed that a centrifugal instability like the one that occurred in Dean's (1928*b*) instability problem was responsible for the appearance of the additional vortices. Near the outer wall, where the axial velocity is decreasing with increasing distance from the centre of curvature of the duct, there is a centrifugally unstable region. If the axial velocity becomes large enough, viscous effects can no longer hold the two-vortex structure in place; thus the additional vortices appear.

The flow development at $Dn = 150$, 137 and 125 showed that the initial flow developments was to a two-vortex structure. At $Dn = 125$, the centrifugal forces are not large enough to cause the formation of the additional vortices, so the two-vortex flow structure remains intact. However, at $Dn = 137$ viscous effects can no longer retain the two-vortex structure, so the additional pair of vortices starts to form. At $Dn = 150$ the centrifugal forces are event stronger, so the formation of the additional vortices starts earlier and their growth rate is faster.

### 4.3. *Development length*

The widely accepted definition of development length is the axial length required for the flow to reach an axially invariant (i.e. fully developed) state. In order to determine if this had been reached, the state of axial velocity at $x'/a = 0.24$ and $z'/a = 0$ was monitored with axial position. Compared to the axial velocities at other duct positions, that at $x'/a = 0.24$ and $z'/a = 0$ experienced the largest change when

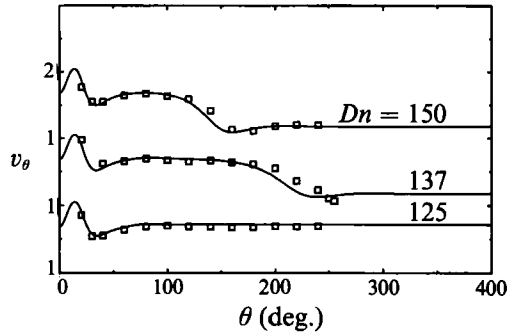


FIGURE 9. Experimentally determined state diagrams (□), with axial velocity at $x'/a = 0.24$ and $z'/a = 0$ as the state variable, compared to the numerically predicted state diagrams (——) of flow development at $Dn = 125$, 137 and 150.

going from a two-vortex to a four-vortex flow, so it was concluded that this location would be the most sensitive to changes in the flow in the axial direction. Comparing the axial velocity development to the radial velocity development at $x'/a = 0.24$ and $z'/a = 0$ suggested that the axial velocity at this location was an accurate indicator of the overall flow development.

Experimentally determined state diagrams for the flow development at $Dn = 125$, 137 and 150 are compared to numerical predictions in figure 9. For $Dn = 125$, the measured flow development is in very good agreement with the numerical simulation. At $Dn = 137$, it is obvious that the flow has not yet reached a fully developed state. After 180°, the state diagram clearly shows that the numerical simulation predicts a faster growth rate of the additional vortex pair. At $Dn = 150$, it is seen that by $\theta = 220°$ the flow has reached an axially invariant state, clearly illustrating the shorter development length at $Dn = 150$ as compared to $Dn = 137$. The axially invariant states predicted by the parabolized three-dimensional formulation were identical to those predicted by the two-dimensional formulation.

For $Dn = 137$, the experimental data in figure 9 show a slower growth rate of the additional vortex pair than predicted by the numerical simulation. Similarly, the state diagram for $Dn = 150$ in figure 9 reveals the same effect at $120° \leqslant \theta \leqslant 160°$; however, the difference between the measured and predicted values is not as large as it was for $Dn = 137$. The better agreement at a larger flow rate suggests that the contribution of the terms neglected in (2.6) to the growth rate of the additional vortex pair becomes less important.

A numerically generated plot of the development length versus Dean number is presented in figure 10. For the two-vortex or two-cell flows the increase of development length with Dean number is linear, while for the four-vortex flows a decrease in development length with increasing Dean number is observed. A sharp increase in development length is seen for the four-vortex or four-cell flows as the Dean number approaches the critical value (i.e. limit point) for the transition from a two-cell to a four-cell flow. The development length appears to approach the critical value asymptotically, indicating an infinite development length at the critical value. This is consistent with the fact that smaller centrifugal forces require a longer axial length for the additional vortices to grow. The critical value predicted by the three-dimensional parabolic simulation has to be slightly less than $Dn = 130$, which was the smallest Dean number at which a four-cell flow was simulated. The critical value for the two-cell to four-cell transition, predicted by the two-dimensional simulation, was around $Dn = 130.9$. The flow visualization studies of Cheng,

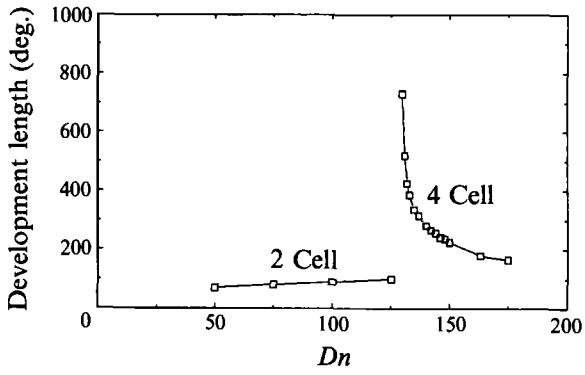


FIGURE 10. Numerical simulation of development length *vs.* Dean number.

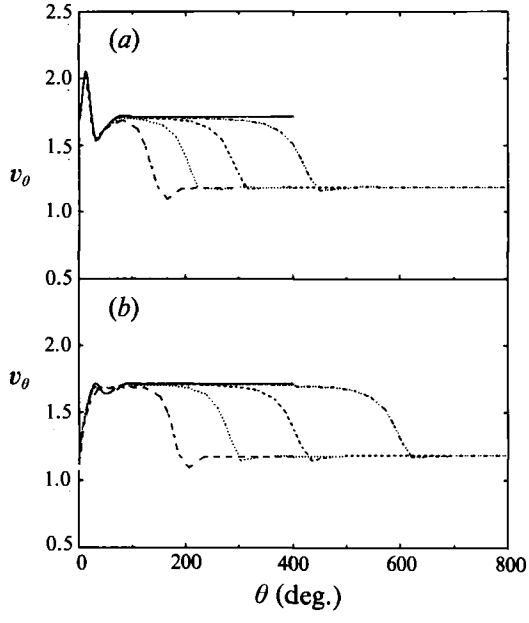


FIGURE 11. Comparison of numerically determined development length for (*a*) a fully developed straight duct inlet profile and (*b*) a uniform inlet profile at $x'/a = 0.24$, $z'/a = 0$: ——, $Dn = 125$; – · · – · · –, 131; – – –, 133; ....., 137; ———, 150.

Nakayama & Akiyama (1979) and Sugiyama *et al.* (1983) of the four-vortex flows in a square duct reveal different sizes of the additional vortex pair depending on Dean number. At the lower Dean numbers the size of the additional vortex pair was smaller. It is important to note that the size of the additional vortex pair should be about the same at all Dean numbers when the flows are fully developed. The behaviour observed in Cheng *et al.* and Sugiyama *et al.* suggests that some of their flows were not fully developed as they had assumed.

In a numerical study of the flow development in a curved duct of square cross-section, Soh (1988) suggested that the flow developed into different states depending on the inlet profile to the curved section. For a fully developed straight duct inlet profile, the flow appeared to develop to a two-vortex-like state, while a free-vortex inlet profile developed into a four-vortex flow. In order to observe the effect that the inlet profile had on the flow development for the curvature ratio used in this study,

a numerical experiment was carried out using a fully developed straight duct inlet profile and uniform inlet profile. Since Agrawal, Talbot & Gong (1978) found that a uniform inlet profile quickly develops into a free vortex, the flow development for a uniform inlet should be very similar to the flow development for a free-vortex inlet.

Figure 11 shows the flow development for a straight duct inlet profile compared to the flow development for a flat inlet profile. For each Dean number simulated, the flow develops to the same final state independent of the initial inlet profile. The four-vortex flows take longer to develop with a uniform inlet profile than with the fully developed straight duct inlet profile. The development to the same state is contrary to what Soh (1988) predicts, but this is easily rationalized as due to insufficient axial length used in his simulations. It is possible that for a larger axial length the same final states might have been observed.

## 5. Investigation of two-dimensional multiple solutions

For fluid flow in a curved duct of square cross-section, Winters (1987) numerically showed that the two-dimensional solution structure was a complex bifurcation diagram with areas of multiple symmetric and asymmetric solutions. A linear stability analysis by Winters also showed that all solutions, except the symmetric two-cell branches, were unstable to perturbations that broke the horizontal symmetry. Even though some of the solutions were also predicted to be unstable to symmetric perturbations, the symmetric four-cell flows were predicted to be stable for a perturbation that did not break the horizontal symmetry.

Given that symmetric four-cell flows were predicted to be unstable to asymmetric perturbations, Winters questioned whether they could be experimentally observed. The results presented in §4.2.3 showed that it is possible to experimentally observe the predicted two-dimensional flow at $Dn = 150$. Even though the four-vortex flow is unstable to asymmetric perturbations, the growth rate of such perturbations must be small if it is possible to observe the flow pattern within the axial length of the apparatus used in this study. The ability to observe the symmetric four-cell flows can be attributed to a combination of an almost perturbation-free inlet profile and slow growth rates of the unstable modes for the four-cell flows. However, it is still in question as to what would happen if enough axial length of the curved section was present for perturbations to grow so their effect could be fully realized.

Using the two-dimensional Navier–Stokes equations given in §2.2, the numerically predicted two-dimensional solution structure as a function of Dean number is shown in figure 12. The solution structure is in the form of a state diagram with the axial velocity at $x'/a = 0.25$ and $z'/a = 0$ as the state variable. The symmetry boundary condition imposed about the horizontal centreline only allowed symmetric solutions to be calculated. Between $Dn = 100$ and 150 it is seen that the solution structure contains a dual solution region with limit points at $Dn \approx 114$ and 131. Winters (1987) showed that the connection between the two-cell and four-cell branches is continuous, but the numerical formulation used in this study was not able to follow the solution around the limit points.

It must be remembered that figure 12 has been calculated for a curved duct of square cross-section with a curvature ratio $R_c = 15.1$. For other curvature ratios the solution structure will have the same appearance, but the location of the limit points will be different. Both Shanthini & Nandakumar (1986) and Winters (1987) have numerically shown that the $Dn$-values of the two limit points increase as the duct becomes more tightly coiled (i.e. as $R_c$ decreases). The two investigations have also

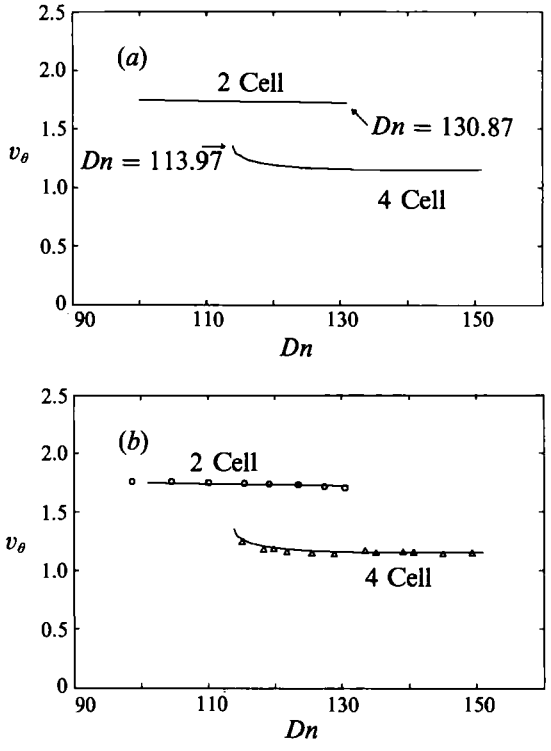


FIGURE 12. State diagram, with axial velocity at $x'/a = 0.25$ and $z'/a = 0$ as the state variable, showing (*a*) the symmetric fully developed two-dimensional solution structure and (*b*) the experimentally determined ($\theta = 220°$) two-dimensional solution structure for a square-cross-section curved duct with $R_c = 15.1$: ○, no pin; △, symmetric pin; ——, numerical prediction.

revealed that when the aspect ratio reaches a value of around 1.4 the two-cell and four-cell branches become disconnected, passing through a transcritical bifurcation.

### 5.1. *Experimental observation of dual solutions*

One of the goals of this study was to experimentally verify the numerically predicted two-dimensional solution structure. An obvious problem in accomplishing this can be seen from figure 10. The lack of sufficient axial development length in the experimental apparatus prevents observation of the naturally developing four-cell flows below $Dn \approx 150$. Given that the measurements in the experimental apparatus were only possible to about 240°, an experimental 'trick' (i.e. pin inserted across the duct; described in §5.3) was required to reduce the development length of the four-cell flows that were below $Dn = 150$.

The experimentally observed two-dimensional solution structure at $\theta = 220°$ is shown in figure 12(*b*). The two-cell branch was determined up to $Dn = 130.5$ by measuring the state variable with no pin inserted at $\theta = 5°$. As will be shown in §5.2, the two-cell to four-cell limit point at $Dn = 130.5$ may or may not actually be a two-cell flow. The entire four-cell branch was observed upon the symmetric insertion of the pin. Starting with a two-cell flow at $Dn \approx 125$, the pin was inserted and adjusted until a symmetric four-cell flow was observed. Once a four-cell flow had been obtained, the flow rate was increased or decreased to trace the solution branch. Using the pin as an experimental trick to observe the four-cell solution branch is consistent with the work of Benjamin (1978*a*, *b*).

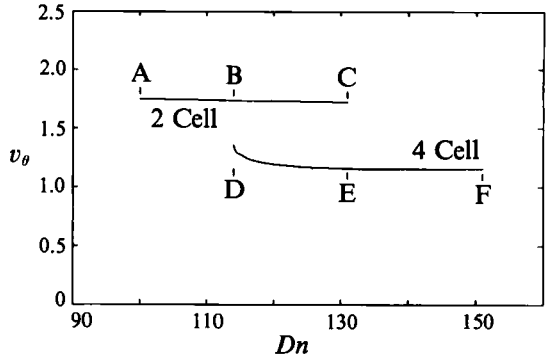


FIGURE 13. State diagram, with axial velocity at $x'/a = 0.25$ and $z'/a = 0$ as the state variable, used to illustrate role of pin in observing different regions of the two-dimensional solution structure: A–B, with and without pin; B–C, only without pin; D–E, only with pin; E–F with pin (without pin not fully developed).

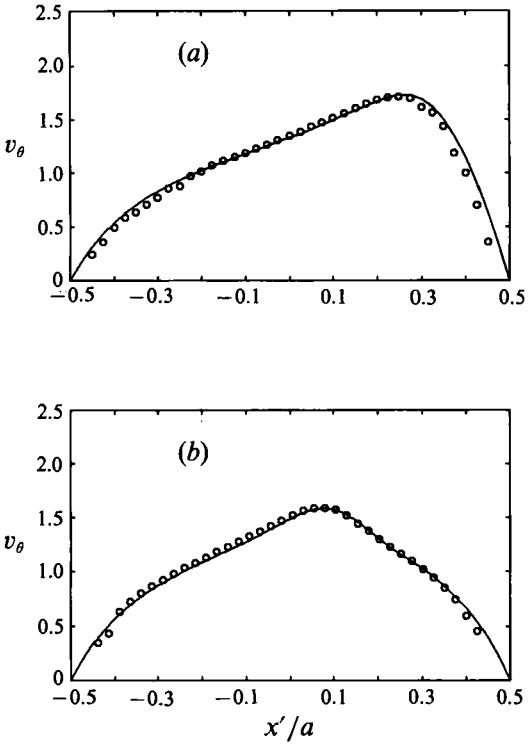


FIGURE 14. Measured axial velocity profiles (○) of a two-cell and four cell flow at $Dn = 125$, and $\theta = 220°$ compared to the numerically predicted fully developed profiles (——). (*a*) Two-cell, (*b*) four-cell.

Figure 13 summarizes the role that the pin played in experimentally observing different regions of the two-dimensional solution structure. The two-cell flows in region A–B and the four-cell flows in region E–F could be observed with and without the pin inserted at the inlet. However, in region E–F the four-cell flows below $Dn \approx 150$ were not fully developed if no pin was used. The four-cell flows in region D–E could only be observed if the pin was used to induce the four-cell flows. Conversely, the two-cells flows in region B–C could only be observed without the pin inserted at the inlet.

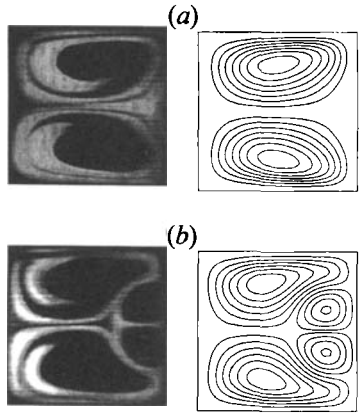


FIGURE 15. Flow visualization of two-cell and four-cell flows at $Dn = 123.4$ compared to numerically predicted secondary flow streamlines. (*a*) Two-cell, (*b*) four-cell.

In figure 12(*b*), the Dean number for the jump from the four-cell branch back to the two-cell branch appears to be close to the numerically predicted value of $Dn \approx 114$. For Dean numbers above about 118, the four-cell flows would remain, but at $Dn = 115.1$ (the lowest experimentally observed value) the four-cell flow was only observed briefly. As the flow rate was decreased below $Dn \approx 118$, the pin (located at $\theta = 5°$) was no longer effective in inducing the four-cell flow, so a two-cell flow developed. However, before the developing two-cell flow reached the downstream measurement position, it appeared that the four-cell structure being convected out of the duct had adjusted to the lower Dean number. Therefore, in order to observe the experimental point at $Dn = 115.1$, the flow rate was reduced and the lowest velocity value was recorded. Since the timescale for the flow to adjust to the lower flow rate was comparable to the convection timescale, the velocity value corresponding to the four-cell flow at $Dn = 115.1$ was only observed for a few seconds.

Figure 14 shows the axial velocity profiles of a two-cell and four-cell flow measured at $Dn = 125$, $\theta = 220°$ and $z'/a = 0$. Flow visualization of the secondary flow patterns at $Dn = 123.4$ are compared to the numerically predicted secondary flow streamlines for a two-cell and four-cell flow in figure 15. From figures 14 and 15 it can be seen that the experimentally observed dual solutions at $Dn \approx 125$ are in very good agreement with the numerical predictions.

### 5.2. *Determining two-cell to four-cell limit point*

Figure 16 shows the naturally occurring solution structure at $\theta = 220°$ if no inlet perturbation is used to induce the two-dimensional four-cell flows below $Dn = 150$. Figures 17(*a*) and 17(*b*) show corresponding arrow plots and flow visualization of the secondary flow structure at $\theta = 220°$. The experimental data in figure 16 were acquired by measuring the axial velocity at $\theta = 220°$, $x'/a = 0.24$ and $z'/a = 0$ while the Dean number was varied. Unlike the numerically generated two-dimensional solution structure, no hysteresis effect was observed when the flow rate was reduced after having obtained a four-cell flow.

From figure 16 it can be seen that at around $Dn = 130$ the value of $v_\theta$ is starting to change in response to the onset of the additional vortex pair. Given that the development length of the four-cell flow is infinite at the critical value, it is difficult

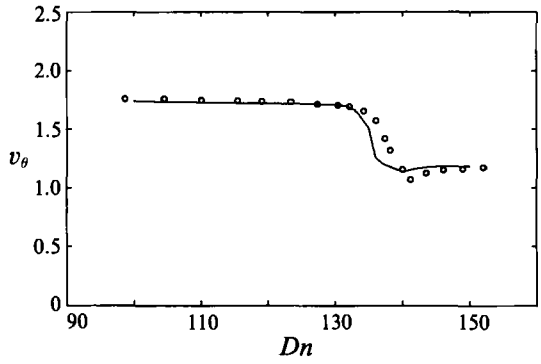


FIGURE 16. State diagram, with axial velocity at $x'/a = 0.24$ and $z'/a = 0$, as the state variable, showing the experimentally (○) and numerically (——) determined naturally occuring solution structure at $\theta = 220°$.

to experimentally determine the two-cell to four-cell limit point. Flow visualization in figure 17 also indicates that the limit point is around $Dn = 130$, but it is impossible to determine a value with a high degree of accuracy. For instance, the flow visualization at $Dn = 129.9$ might represent a four-vortex flow where the additional vortices have not yet started to grow. Based on the axial velocity measurements and flow visualization, a best estimate of the experimentally determined two-cell to four-cell limit point is $Dn = 130 \pm 1$–$2\%$.

The numerical curve in figure 16 was generated by performing a developing flow simulation for each of a series of Dean numbers between 100 and 150. Once a developing flow simulation had been completed, the axial velocity at $\theta = 220°$, $x'/a = 0.24$ and $z'/a = 0$ was extracted and used in the construction of the state diagram. The difference between the numerical prediction and measurements in the region between $Dn = 133$ and 145 is a result of the numerical simulation predicting a faster growth rate of the additional vortices. This effect can also be seen by comparing the arrow plots and flow visualization in figures 17(*a*) and 17(*b*) respectively. A feature that is common to the three-dimensional numerical simulation and the experimental measurements is the difficulty in determining the Dean number of the two-cell to four-cell limit point.

### 5.3. *Reduction of development length*

As seen in §5.1, the fully developed four-cell flows at Dean numbers below about 150 were observed by introducing a perturbation at 5° downstream from the curved section inlet. A 0.4 mm diameter pin was inserted across the duct on a radial line at the duct's horizontal axis of symmetry ($z'/a = 0$). The appearance of the four-cell flows was very sensitive to the positioning of the pin. If the pin did not cause a symmetric perturbation, then the fully developed symmetric four-cell flows could not be observed.

The size of the pin was kept small enough so that no undesirable effects were introduced from its wake. Assuming that the pin would see a maximum velocity equal to the value at the duct centre of the straight section inlet, the pin Reynolds number, $Re_{\text{pin}}$ (based on the pin's diameter) was 39 at $Dn = 150$. For $Re_{\text{pin}}$ less than about 60, Schlichting (1979) states that the wake behind a circular cylinder will be laminar with no appearance of a Kármán vortex street. Since the pin was not subjected to a Dean number higher than $Dn = 150$, the wake behind the pin would always be free of a vortex street.

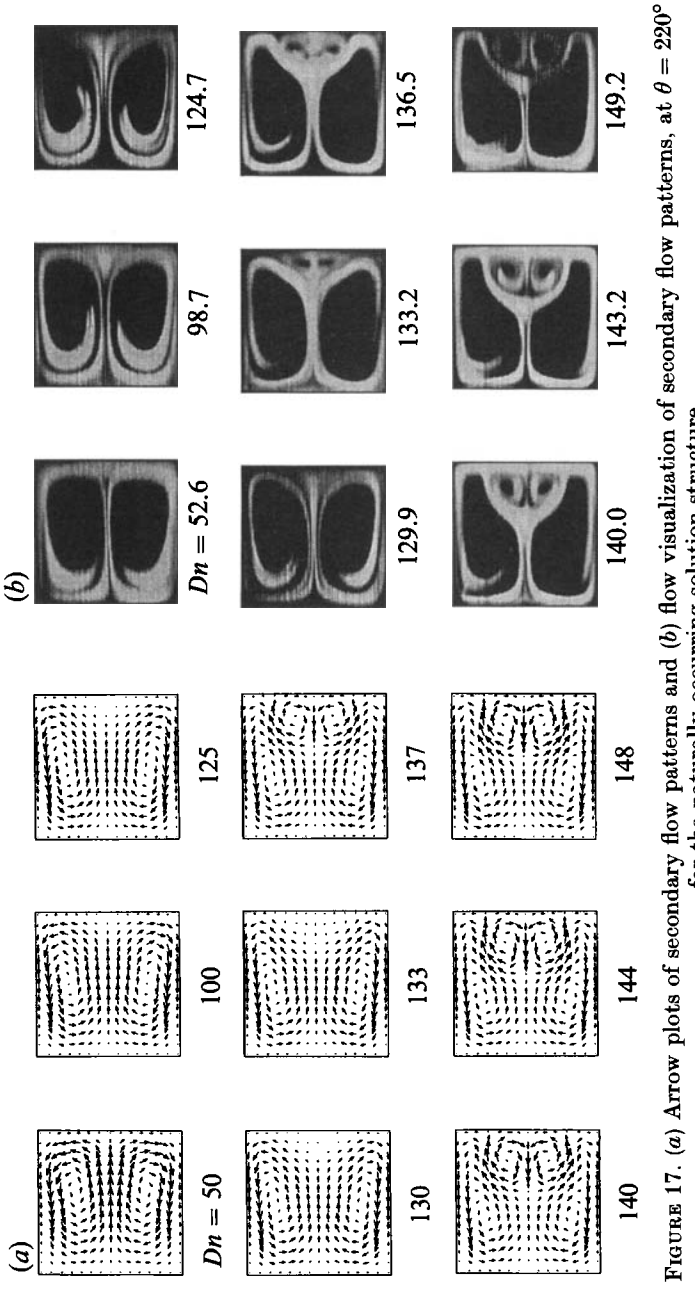


FIGURE 17. (*a*) Arrow plots of secondary flow patterns and (*b*) flow visualization of secondary flow patterns, at $\theta = 220°$ for the naturally occurring solution structure.

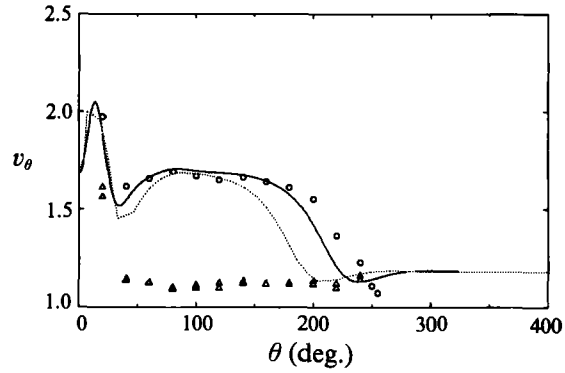


FIGURE 18. State diagram, with axial velocity at $x'/a = 0.24$ and $z'/a = 0$ as the state variable, showing the reduction in development length at $Dn = 137$ for an experimental and numerical symmetric trip. Experimental: ○, no trip; △, symmetric trip. Numerical: ——, no trip; ....., symmetric trip.

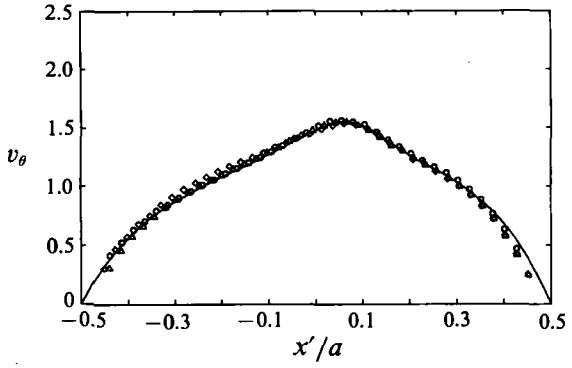


FIGURE 19. Measured axial velocity profiles, at $Dn = 137$, $\theta = 60°$ (◇), 140° (△), 220° (○) and $z'/a = 0$, with a symmetric trip at $\theta = 5°$ compared to numerically calculated fully developed profile.

The effect of a pin placed symmetrically across the duct at $Dn = 137$ can be seen in figure 18. The circles are the measured flow development with no pin and the triangles show the flow development for the symmetrically placed pin. With the pin, the flow appears to have already become axially invariant by about $\theta = 40°$. Measured velocity profiles at $Dn = 137$ and $\theta = 60°$, 140° and 220° compared to the numerically calculated two-dimensional profile in figure 19, verify that the flow throughout most of the duct's axial length is axially invariant.

The symmetric trip was numerically modelled by setting the axial and radial velocity components to zero at the grid points on the duct's horizontal axis of symmetry. This was done at $\theta = 5°$ once a converged profile had already been obtained. The dotted line in figure 18 shows the numerically predicted flow development with a symmetric trip compared to the experimentally measured development with the symmetrically positioned pin (i.e. symmetric trip). The numerical simulation shows a reduced development length, but it nowhere near to what was measured. The difference is because the numerical trip (i.e. setting the velocities at $-0.5 \leqslant x'/a \leqslant 0.5$ and $z'/a = 0$ to zero) is not an accurate model of the pin's effect.

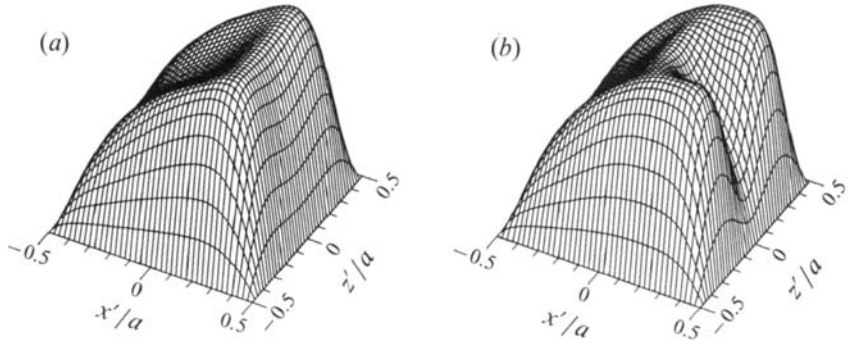


FIGURE 20. Three-dimensional axial velocity plot of fully developed (*a*) two-cell and (*b*) four-cell flows at $Dn = 123.4$.

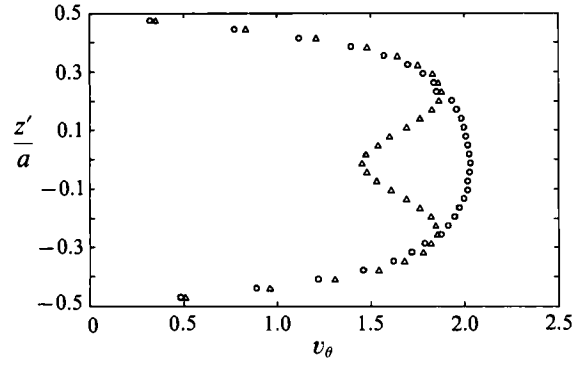


FIGURE 21. Measured axial velocity profile at $Dn = 125$, $\theta = 20°$ and $x'/a = 0.32$ with (△) and without (○) a symmetric pin at $\theta = 5°$.

### 5.4. *Role of the pin in inducing four-vortex flows*

The role of the pin in inducing the four-cell flows can be explained with the aid of the three-dimensional plots of axial velocity in figure 20. The two-cell and four-cell axial velocity surfaces were numerically calculated using the two-dimensional vorticity–stream-function formulation of §2.2. The major difference between the two-cell and four-cell velocity surfaces is the depression at the horizontal line of symmetry in the four-cell one. The velocity gradients near the outer wall in the four-cell profile are necessary if the additional pair of vortices is to exist. In fact, the vorticity transport equation (2.14) reveals that it is the gradients of the axial velocity in the vertical direction that drive the secondary flow.

Figure 21 shows the measured axial velocity profiles in the vertical direction at $Dn = 125$, $\theta = 20°$ and $x'/a = 0.32$ with and without the pin. Without the pin the profile is fairly uniform in the central region. However, upon the insertion of the symmetrically placed pin, the profile develops a depression. The vertical axial velocity gradients induced by the pin's presence cause the additional vortices to form at the outer wall. Given that the pin's role is to create the proper velocity gradients, its axial position should not be critical.

## 6. Response of flow to asymmetric perturbations

The numerical studies of Winters (1987) and Yanase *et al.* (1988) demonstrated that the fully developed four-cell flows in curved ducts of both rectangular and circular cross-section are unstable to asymmetric perturbations. In each case the

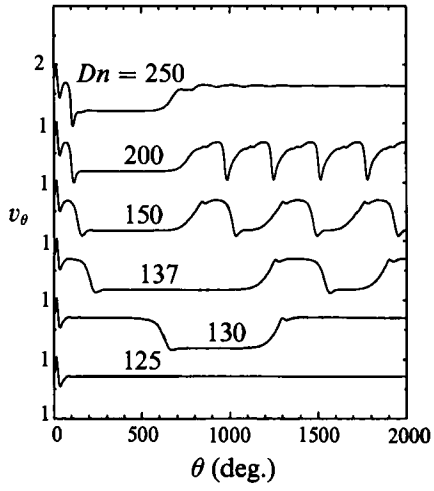


FIGURE 22. Numerically calculated state diagrams, with axial velocity at $x'/a = 0.24$ and $z'/a = 0$ as the state variable, showing flow development to $\theta = 2000°$ at $Dn = 125$, 130, 137, 150, 200 and 250.

four-cell flows were found to be stable for a symmetric disturbance, while the two-cell flows were found to be stable for any arbitrary disturbance. The use of a symmetric pin to experimentally induce the fully developed four-cell flows, as was shown in §5.3, is consistent with Winter's prediction that such flows are stable to symmetric disturbances.

In §5.1 it was shown that for $Dn \leqslant 150$, the symmetric four-cell flows predicted by the two-dimensional Navier–Stokes equations could be experimentally observed within 240° of axial length. Given that fully developed four-cell flows are unstable to asymmetric perturbations, and that any experimental apparatus will have inherent asymmetries, suggests that the growth rate of such disturbances must be small in order to experimentally observe the flows. If an asymmetric disturbance is not introduced at the inlet, naturally occurring asymmetries might require large axial lengths before their effects are observed. However, whether an asymmetric disturbance of significant magnitude is deliberately introduced at the inlet or allowed to grow naturally, the question still remains as to what happens to the flow under the influence of asymmetric perturbations.

For the range of Dean numbers investigated in the curved duct, the inlet flows were steady. However, one possible way that the four-cell flows could respond to growing asymmetric perturbations is to develop time-dependent fluctuations. In order to check the steadiness of the flows that were investigated, a point at $\theta = 240°$ was chosen, and the axial velocity was monitored for at least 80 minutes. The velocity was monitored on the horizontal line of symmetry (i.e. $z'/a = 0$) and at one quarter of the duct width from the outer wall (i.e. $x'/a = 0.25$). For the four-cell flows, this position was between the additional vortex pair at the outer wall, so any motion in the vortices should easily be detected. None of the flows measured in the curved duct showed any time dependence.

### 6.1. *Numerical investigation of flow behaviour at large axial distances*

In the experimental apparatus used in this study, measurement of the flow development was limited to an axial length of around 240°. This amount of axial length was not sufficient to determine the ultimate state of the four-cell flows under

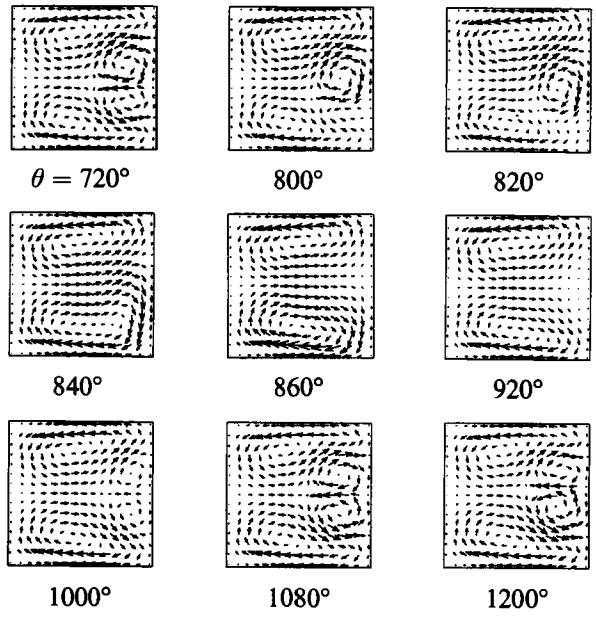


FIGURE 23. Arrow plots of spatial oscillations at $Dn = 150$ showing the development of the secondary flow between $\theta = 720°$ and 1200°.

the influence of any asymmetric perturbations. Therefore, in order to conjecture what might happen, a numerical investigation of the flow development to large axial lengths was performed. In the numerical simulations asymmetric perturbations arise naturally due to round-off errors. Figure 22 shows state diagrams of the numerically simulated flow development at $Dn = 125$, 130, 137, 150, 200 and 250.

It is seen that at $Dn = 125$ the flow remains axially invariant after $\theta \approx 100°$. It is not surprising that the two-cell flow remains axially invariant, since it is supposedly stable to any arbitrary perturbation. In contrast, the four-cell flows at $Dn = 130$, 137, 150 and 200 eventually develop a spatial oscillations in the streamwise direction. The frequency of these oscillations increased as the Dean number was increased. As shown by Sankar *et al.* (1988), these oscillations are not a numerical artifact. They repeated some calculations with different axial step sizes and cross-plane grid resolution and found that the nature of the oscillations and periods were sustained.

The oscillations in the axial velocity are a result of oscillations in the additional pair of vortices at the outer wall. Figure 23 shows arrow plots of the secondary flow corresponding to the state diagram of axial velocity at $Dn = 150$ shown in figure 22. The arrow plot at $\theta = 720°$ reveals a growing asymmetry in the additional vortex pair as the vortices move downward in the cross-section. The top cell appears to increase in size slightly while the bottom cell is compressed into the corner. The increase in axial velocity between $\theta = 600°$ and 780°, in the state diagram at $Dn = 150$, reflects the growing asymmetry of the additional vortex pair.

In the region from $\theta = 800°$ to 860°, the additional vortex pair disappears into the bottom vortex of the larger pair. By $\theta = 920°$ the larger vortex pair has readjusted to what appears to be a symmetric two-cell flow. The axial velocity at $\theta = 920°$, as seen in the state diagram at $Dn = 150$, has a value that is typical of a two-cell flow. After $\theta = 920°$, the additional vortex pair reappears and continues to grow in size until $\theta = 1080°$, where a small vertical velocity in the upward direction is evident in the secondary velocity vectors on the horizontal line of symmetry near the outer

wall. Following the flow development to $\theta = 1200°$, it is seen that the asymmetry in the additional vortex pair grows as before, but the movement of the cells is now toward the top of the duct. The alternating movement of the additional vortices from top to bottom results in a period that is twice as long as the period for axial velocity shown in figure 22, and is a consequence of the symmetries in the governing equations. If the axial velocities in figure 22 had been monitored off the horizontal line of symmetry then they would have shown the longer period of oscillation.

The oscillation of the flow between a two-cell and four-cell state is consistent with Winter's prediction that there is no stable two-dimensional flow in the region immediately beyond the limit point of the two-cell to four-cell transition. Once the limit point is exceeded and a four-cell flow develops, numerical round-off introduces asymmetries which cause the additional vortex pair at the outer wall to experience a spatial oscillation in the streamwise direction. Sankar *et al.* (1988) found that their four-cell flows at $Dn = 200$, for curvature ratios $R_c = 4$ and 10, remained axially invariant up to $\theta = 2500°$. However, after rerunning their simulations for larger axial lengths, it was found that sustained oscillations appeared.

In the state diagram of figure 22, the numerical simulation shows that at $Dn = 250$ the flow appears to eventually develop into an axially invariant two-cell state. The numerical study of Winters (1987) revealed that an isolated two-cell branch exists at this higher Dean number, so it is possible that the flow has been attracted to this state. Winters also predicted that the isolated two-cell branch was stable to any arbitrary perturbation. The breakdown of the four-cell flow to what appears to be an axially invariant two-cell state at $Dn = 250$ is consistent with the solution structure and stability characteristics predicted by Winters.

The above phenomena of a four-cell flow giving way to a stable two-cell flow also happens in the dual solution region between $Dn \approx 114$ and 130. Figure 24 shows the numerical prediction of flow development at $Dn = 110$, 125 and 137 with a four-cell flow inlet profile. The inlet profile used was the axially invariant four-cell profile calculated in the flow development simulation at $Dn = 150$. At $Dn = 110$, the two-cell flow is the unique solution to the two-dimensional equations, so the flow quickly evolves to the two-cell state. After an initial adjustment region, the four-cell flow at $Dn = 125$ is axially invariant for about 500° before giving way to a two-cell flow. The use of a four-cell flow as the inlet profile was the only way that the dual solutions could be observed with the three-dimensional numerical formulation. The familiar spatial oscillation is again seen at $Dn = 137$, once the limit point (i.e. point C of figure 13) of the two-cell to four-cell transition is exceeded.

The numerical investigation of flow development is consistent with the prediction that fully developed four-cell flows are unstable to asymmetric perturbations. In the regions of dual solutions, it was seen that the four-cell flow would give way to a stable two-cell flow. For Dean numbers where no stable two-dimensional solutions exist, the flows might develop spatial oscillations or time dependence, or even some combination of the two. In the numerical study of Finlay, Keller & Ferziger (1988) for flow in a curved channel of infinite span, they found that travelling waves developed in the streamwise direction at higher Reynolds numbers. Their observation suggests that the same type of phenomena might be possible in a curved duct of finite aspect ratio. It must be kept in mind that the three-dimensional numerical formulation used in this study does not model time dependence, so the instabilities in the four-cell flows were forced to show up as spatial oscillations.

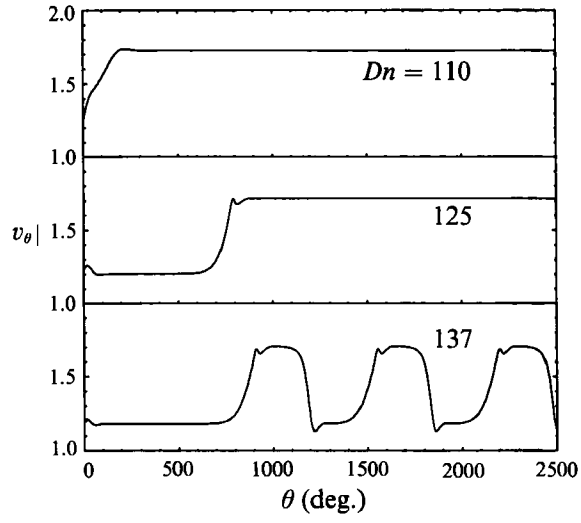


FIGURE 24. Numerically calculated state diagram, with axial velocity at $x'/a = 0.24$ and $z'/a = 0$ as the state variable, showing flow development to $\theta = 2500°$ at $Dn = 110$, 125 and 137 with a developed four-cell flow as the inlet condition.

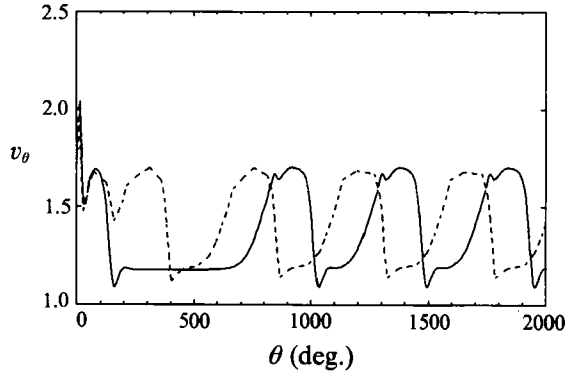


FIGURE 25. Numerically calculated state diagram, with axial velocity at $Dn = 150$, $x'/a = 0.24$ and $z'/a = 0$ as the state variable, showing flow development with (----) and without (——) an asymmetric perturbation at $\theta = 5°$.

### 6.2. *Experimental evidence of streamwise spatial oscillations*

The numerical investigation of §6.1 showed that, given enough axial length, asymmetries will develop and cause streamwise spatial oscillations. However, there is still some doubt as to whether the flow will behave like that in the real situation. In order to study this, asymmetric perturbations were deliberately introduced at the inlet of the experimental apparatus in the hope of observing some far downstream behaviour within the axial length of the apparatus.

In order to gain some insight into the effect of an asymmetric perturbation at the inlet, a numerical simulation was performed. Figure 25 shows a state diagram of the flow development at $Dn = 150$ for an asymmetric perturbation at $\theta = 5°$. The asymmetric perturbation was accomplished by setting the axial and radial velocities at $z'/a = 0.034$ to zero. This was done at all grid points across the width of the duct (i.e. $-0.5 \leqslant x'/a \leqslant 0.5$). The simulation reveals that an asymmetric perturbation at

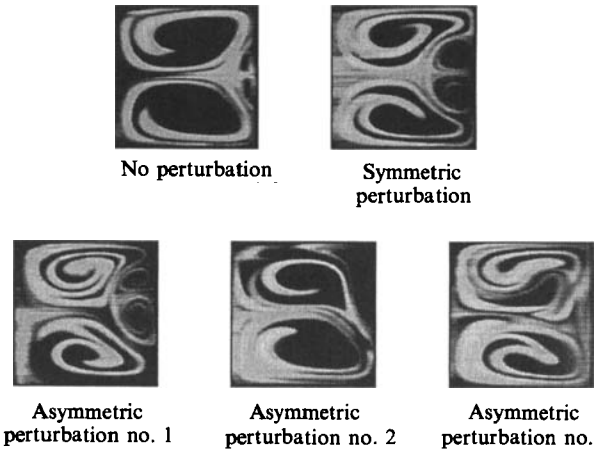


FIGURE 26. Flow visualization of secondary flow patterns at $Dn = 133.9$ and $\theta = 220°$ showing the effect of different perturbations at $\theta = 5°$.

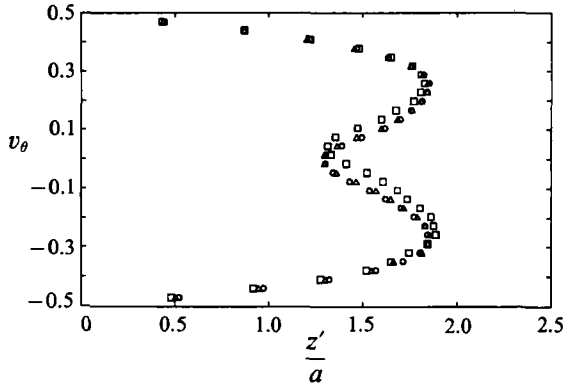


FIGURE 27. Vertical profiles of axial velocity measured at $Dn = 133.9$, $\theta = 20°$ and $x'/a = 0.32$ showing the degree of asymmetry in the axial velocity profile for different perturbations: ○, symmetric; △, asymmetric 1; □, asymmetric 3.

the inlet results in the earlier appearance of the sustained spatial oscillations. It is easy to imagine that for different degrees of asymmetry in the inlet perturbation, the axial position of the spatial oscillations would correspondingly shift. Therefore, the spatial oscillation could be observed at one axial location by shifting the axial position of the oscillation with different asymmetric perturbations.

Varying degrees of asymmetry were introduced in the experimental apparatus by rotating the pin. Small rotations of the pin, resulting in small vertical movements, broke the symmetry of the flow about the horizontal centreline (i.e. $z'/a = 0$). In figure 26, flow visualization of the secondary flow patterns at $Dn = 133.9$ and $\theta = 220°$ show the patterns for various perturbations at $\theta = 5°$. As expected, with no perturbation at $\theta = 5°$, a developing four-cell flow is observed at $\theta = 220°$. Also, a symmetric perturbation at $\theta = 5°$ resulted in a developed four-cell flow at $\theta = 220°$. The three asymmetric perturbations, identified as 1, 2 and 3, have an increasing degree of asymmetry associated with them. This can be seen from the vertical profiles of axial velocity at $\theta = 20°$ presented in figure 27. The small difference between the

axial velocity profiles of the symmetric perturbation and asymmetric perturbation 1, reveals the sensitivity of the secondary flow pattern observed at $\theta = 220°$ to the position of the pin.

Figure 26 shows that the three asymmetric perturbations cause an increasing asymmetry of the additional vortex pair at $\theta = 220°$ until they finally disappear into the top vortex. The progression actually happens in space. However, by manipulation of the pin at $\theta = 5°$ the progression can be observed at one axial location. Using a portable laser light sheet (based on Koga, Abrahamson & Eaton 1987), the increasing asymmetry in the additional vortex pair and its subsequent disappearance into the larger vortex, as shown in figure 26, was observed within an axial length of about 40°. This is in very good agreement with the behaviour shown by the three arrow plots at $\theta = 800°$ to 840° in figure 23. The secondary flow structures at $\theta = 220°$, caused by the asymmetric perturbations, did not display any time dependence. This confirms that within the axial length of the experimental apparatus, there exists a streamwise spatial variation that resembles the numerically predicted spatial oscillation.

For the conditions of an asymmetric trip at $\theta = 5°$, figure 28 shows a comparison between the experimentally measured state diagram of flow development at $Dn = 137$ and the corresponding numerical prediction. The top graph shows that the asymmetric perturbation in the numerical simulation does not model the asymmetric perturbation caused by the pin in the experiment. The same inability to model the pin was observed for the case of the symmetric pin in figure 18. However, by shifting the numerically predicted curve 225° to the left as shown in the bottom graph of figure 28, the numerical prediction agrees quite well with the measured data. The fact that part of a streamwise spatial oscillation is observable in the experimental apparatus suggests that sustained streamwise spatial oscillations may not be merely an artifact of the steady, parabolized formulation.

## 7. Conclusions

Axial velocity profiles of flow development were measured every 20° up to an axial length of $\theta = 240°$ at $Dn = 125$, 137 and 150 for a square duct of curvature ratio, $R_c = 15.1$. As expected, the flow at $Dn = 125$ developed into a symmetric two-vortex flow. Measurement of vertical velocity profiles and flow visualization confirmed the symmetry of the flow. At $Dn = 150$, the flow developed into a fully developed symmetric four-vortex state. Flow visualization and measured vertical velocity profiles verified that the flow was symmetric. The axial velocity measurements and flow visualization at $Dn = 137$ revealed that by $\theta = 240°$ the flow had not yet reached a fully developed state. Numerical simulations of the flow development at $Dn = 125$, 137 and 150, using a steady three-dimensional parabolized formulation of the Navier–Stokes equations, were in good agreement with measured axial velocities. Measurement of a developing four-vortex flow to its fully developed state (i.e. at $Dn = 150$) was accomplished for the first time in this study. Also, the discovery of the decrease of the development length with increasing Dean number for the four-vortex flows has not been previously reported.

Given that the development length of the four-cell flows decreased with increasing Dean number, a numerical investigation for Dean numbers below $Dn = 175$ was performed to reveal more detail. At the limit point of the two-cell to four-cell transition the development length appeared to be infinite, while at $Dn = 175$ the development length was calculated to be about 165°. The faster development of the additional vortices for a larger centrifugal force (i.e. larger $Dn$), is consistent with the

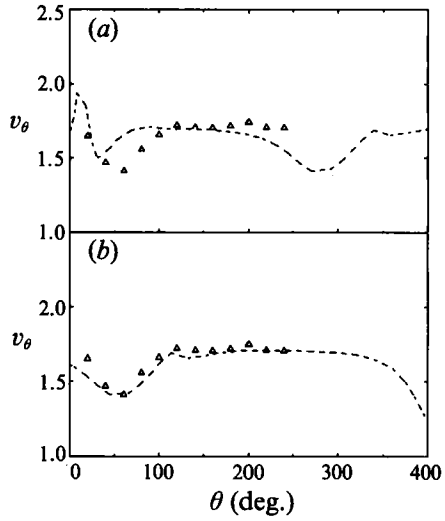


FIGURE 28. Measured state diagram (△), with axial velocity at $Dn = 137$, $x'/a = 0.24$ and $z'/a = 0$ as the state variable, compared to the numerically calculated state diagram with an asymmetric perturbation at $\theta = 5°$ (----). In (*b*) the numerical curve has been shifted 225° to the left in order to line up with the measured data.

suggestion of Cheng *et al.* (1976) that the formation of the additional vortex pair is due to a centrifugal instability.

Using a symmetrically positioned pin at $\theta = 5°$ to induce the four-cell flows, it was shown for the first time that the predicted symmetric two-dimensional solution structure for $Dn \leqslant 150$ could be experimentally observed. The pin reduced the development length of the four-cell flows, allowing the two-dimensional solutions to be observed within the 240° axial length of the experimental apparatus. The experimentally determined limit points of the two-cell to four-cell transition and the four-cell to two-cell transition were in good agreement with the numerically predicted values of $Dn \approx 131$ and 114 respectively. Axial velocity profiles and flow visualization were taken of a dual solution at $Dn = 123.4$.

Winters (1987) numerical prediction that fully developed four-cell flows are stable to symmetric perturbations, but unstable to asymmetric perturbations, was found to be consistent with the present experimental observations. A symmetrically positioned pin was able to induce a fully developed symmetric four-cell flow. Numerical simulations revealed that under the influence of asymmetric perturbations, four-cell flows develop sustained streamwise spatial oscillations in those regions where there are no stable two-dimensional solutions. In the dual solution region, the numerical simulations showed that the four-cell flow would give way to a stable two-cell flow. An experimental investigation showed the existence of a time-independent spatial variation resembling the initial part of a numerically predicted streamwise spatial oscillation. The spatial variation was observed within the axial length of the apparatus by deliberately inserting asymmetric perturbations at $\theta = 5°$.

Given that the fully developed four-cell flows are unstable to asymmetric perturbations, the question as to what happens to the flows farther downstream still exists. The parabolized steady three-dimensional equations used for the numerical simulations were restricted to show instabilities in space, so they could not predict any time-dependent motions. Even though no time dependence was observed in the

flows measured within the axial length of the experimental apparatus, it is possible that the unstable four-cell flows might develop time dependence farther downstream. It would be expected that the growth rate of the asymmetric disturbances would increase with increasing Dean number. Therefore, experiments at higher Dean numbers might show time dependence within the axial length of the present apparatus. In order to numerically determine time-dependent behaviour, a numerical formulation would be required that retained the time-dependant terms.

An equipment grant from the Natural Sciences and Engineering Research Council (NSERC) was crucial in developing the experimental facilities used in this work. Continuing operating grants to K.N. and J.H.M. from NSERC and graduate fellowships to B.B. from NSERC and the Province of Alberta are gratefully acknowledged. The assistance in the experimental part of the work from Mr. John VanDoorn and the interest and advice from Professor D. J. Wilson are much appreciated.

## REFERENCES

AGRAWAL, Y., TALBOT, L. & GONG, K. 1978 Laser anemometer study of flow development in curved circular pipes. *J. Fluid Mech.* **85**, 497–518.

AKIYAMA, M. 1969 Laminar forced convection heat transfer in curved rectangular channels. M.Sc. thesis, Mechanical Engineering Department, University of Alberta.

AUSTIN, L. R. & SEADER, J. D. 1974 Entry region for steady viscous flow in coiled circular pipes. *AIChE J.* **20**, 820–822.

BARA, B. 1991 Experimental Investigation of developing and fully developed flow in a curved duct of square cross section. Ph.D. thesis, Mechanical Engineering Department, University of Alberta.

BEAVERS, G. S., SPARROW, E. M. & MAGNUSON, R. A. 1970 Experiments on hydrodynamically developing flow in rectangular ducts of arbitrary aspect ratio. *Intl J. Heat Mass Transfer* **13**, 689–702.

BENJAMIN, T. B. 1978*a* Bifurcation phenomena in steady flows of a viscous fluid, I. Theory. *Proc. R. Soc. Lond.* A. **359**, 1–26.

BENJAMIN, T. B. 1978*b* Bifurcation phenomena in steady flows of a viscous fluid, II. Experiments. *Proc. R. Soc. Lond.* A. **359**, 27–43.

BERGER, S. A., TALBOT, L. & YAO, L.-S. 1983 Flow in curved pipes. *Ann. Rev. Fluid Mech.* **15**, 461–512.

CAMPBELL, R. 1991 Image processing techniques for analysis of full color turbulent jet images. M.Sc. thesis, Mechanical Engineering Department, University of Alberta.

CHENG, K. C. & AKIYAMA, M. 1970 Laminar forced convection heat transfer in curved rectangular channels. *Intl J. Heat Mass Transfer* **13**, 471–490.

CHENG, K. C., LIN, R-C. & OU, J-W. 1975 Graetz problem in curved square channels. *Trans. ASME* C: *J. Heat Transfer* **97**, 244–248.

CHENG, K. C., LIN, R-C. & OU J-W. 1976 Fully developed laminar flow in curved rectangular channels. *Trans. ASME* C: *J. Fluids Engng.* **98**, 41–48.

CHENG, K. C., NAKAYAMA, J. & AKIYAMA, M. 1979 Effect of finite and infinite aspect ratios on flow patterns in curved rectangular channels. In *Flow Visualization*, pp. 181–186. Hemisphere.

CHENG, K. C. & YEUN, F. P. 1987 Flow visualization studies on secondary flow patterns in straight tubes downstream of a 180 deg bend and in isothermally heated horizontal tubes. *Trans. ASME* C: *J. Heat Transfer* **109**, 49–54.

CUMING, H. G. 1952 The secondary flow in curved pipes. *Aeronaut. Res. Counc. Rep. Mem.*, No. 2880.

DASKOPOULOS, P. & LENHOFF, A. M. 1989 Flow in curved ducts: bifurcation structure for stationary ducts. *J. Fluid Mech.* **203**, 125–148.

DEAN, W. R. 1927 Note on the motion of fluid in a curved pipe. *Phil. Mag.* (7) **4**, 208–223.

DEAN, W. R. 1928*a* The stream-line motion of fluid in a curved pipe. *Phil. Mag.* (7) **5**, 673–695.

DEAN, W. R. 1928*b* Fluid motion in a curved channel. *Proc. R. Soc. Lond.* A **121**, 402–420.

DENNIS, S. R. C. & NG, M. 1982 Dual solutions for steady laminar flow through a curved tube. *Q. J. Mech. Appl. Maths* **35**, 305–324.

EUSTICE, J. 1910 Flow of water in curved pipes. *Proc. R. Soc. Lond.* A **84**, 107–118.

EUSTICE, J. 1911 Experiments on stream-life motion in curved pipes. *Proc. R. Soc. Lond.* A **85**, 119–131.

EUSTICE, J. 1925 Flow of fluids in curved passages. *Engineering* Nov. 13, pp. 604–605.

FINLAY, W. H., KELLER, J. B. & FERZIGER, J. H. 1988 Instability and transition in curved channel flow. *J. Fluid Mech.* **194**, 417–456.

GHIA, K. N. & SOKHEY, J. S. 1977 Laminar incompressible viscous flow in curved ducts of regular cross-section. *Trans. ASME* I: *J. Fluids Engineering* **99**, 640–648.

GOLDSTEIN, R. J. & KREID, D. K. 1967 Measurement of laminar flow development in a square duct using a laser-doppler flowmeter. *Trans. ASME* E: *J. Appl. Mech.* **34**, 813–818.

HILLE, P., VEHRENKAMP, R. & SCHULZ-DUBOIS, E. O. 1985 The development and structure of primary and secondary flow in a curved square duct. *J. Fluid Mech.* **151**, 219–241.

HUMPHREY, J. A. C., TAYLOR, A. M. K. & WHITELAW, J. H. 1977 Laminar flow in a square duct of strong curvature. *J. Fluid Mech.* **83**, 509–527.

ITŌ, H. 1951 Theory on laminar flow through curved pipes of elliptic and rectangular cross-sections. *Rep. Inst. High Speed Mech., Tohoku Univ., Sendai Japan*, vol. 1, pp. 1–16.

ITŌ, H. 1987 Flow in curved pipes. *JSME Int. J.* **30**, 543–552.

JOSEPH, B., SMITH, E. P. & ALDER, R. J. 1975 Numerical treatment of laminar flow in helically coiled tubes of square cross section. Part 1. Stationary helically coiled tubes. *AIChE J.* **21**, 965–974.

KAJISHIMA, T., MIYAKE, Y. & INABA, T. 1989 Numerical simulation of laminar flow in curved ducts of rectangular cross section. *JSME Intl J.* **32**, 516–522.

KOGA, D. J., ABRAHAMSON, S. D. & EATON, J. K. 1987 Development of a portable laser sheet. *Expts. Fluids* **5**, 215–216.

MASLIYAH, J. H. 1980 On laminar flow in curved semicircular ducts. *J. Fluid Mech.* **99**, 469–479.

NANDAKUMAR, K. & MASLIYAH, J. H. 1982 Bifurcation in steady laminar flow through curved tubes. *J. Fluid Mech.* **119**, 475–490.

NANDAKUMAR, K. & MASLIYAH, J. H. 1986 Swirling flow and heat transfer in coiled and twisted pipes. In *Advances in Transport Processes*, vol. 4, pp. 49–112. Wiley Eastern.

NANDAKUMAR, K., RASZILLIER, H. & DURST, F. 1991 Flow through rotating rectangular ducts. *Phys. Fluids* A **3**, 770–781.

NANDAKUMAR, K. & WEINITSCHKE, H. J. 1991 A bifurcation study of mixed convection heat transfer in horizontal ducts. *J. Fluid Mech.* **231**, 157–187.

PATANKAR, S. V. 1980 *Numerical Heat Transfer and Fluid Flow.* Hemisphere.

SANKAR, S. R., NANDAKUMAR, K. & MASLIYAH, J. H. 1988 Oscillatory flows in coiled square ducts. *Phys. Fluids* **31**, 1348–1358.

SCHLICHTING, H. 1979 *Boundary-Layer Theory* (7th edn). McGraw-Hill.

SHAH, R. K. & LONDON, A. L. 1978 *Laminar Flow Forced Convection in Ducts.* Academic.

SHANTHINI, W. 1985 Bifurcation phenomena of generalized newtonian fluids in curved rectangular ducts. M.Sc. thesis, Chemical Engineering Department, University of Alberta.

SHANTHINI, W. & NANDAKUMAR, K. 1986 Bifurcation phenomena of generalized newtonian fluids in curved rectangular ducts. *J. Non-Newtonian Fluid Mech.* **22**, 35–60.

SOH, W. Y. 1988 Developing fluid flow in a curved duct of square cross-section and its fully developed dual solutions. *J. Fluid Mech.* **188**, 337–361.

SUGIYAMA, S., HAYASHI, T. & YAMAZAKI, K. 1983 Flow characteristics in the curved rectangular channels (visualization of secondary flow). *Bull. JSME* **26**, 964–969.

SUGIYAMA, S., AOI, T., YAMAMOTO, M. & NARISAWA, N. 1989 Measurements of developing laminar flow in a curved rectangular duct by means of LDV. In *Experimental Heat Transfer, Fluid Mechanics and Thermodynamics*, (ed. R. K. Shah *et al.*), pp. 1185–1191. Elsevier.

TAYLOR, A. M. K. P., WHITELAW, J. H. & YIANNESKIS, M. 1982 Curved ducts with strong secondary motion: velocity measurements of developing laminar and turbulent flow. *Trans. ASME* I: *J. Fluids Engng.* **104**, 350–359.

THOMSON, J. 1876 On the origin windings of rivers in alluvial plains, with remarks on the flow of water round bends in pipes. *Proc. R. Soc. Lond.* A **25**, 5–8.

WEINITSCHKE, H. J., NANDAKUMAR, K. & SANKAR, S. R. 1990 A bifurcation study of convective heat transfer in porous media. *Phys. Fluids* A **2**, 912–921.

WILLIAMS, G. S., HUBBELL, C. W. & FINKELL, G. H. 1902 Experiments at Detroit, Michigan on the effect of curvature on the flow of water in pipes. *Trans. ASCE* **47**, 1–196.

WINTERS, K. H. 1987 A bifurcation study of laminar flow in a curved tube of rectangular cross-section. *J. Fluid. Mech.* **180**, 343–369.

WINTERS, K. H. & BRINDLEY, R. C. G. 1984 19 Multiple solutions for laminar flow in helically-coiled tubes *AERE Rep.* 11373. AERE Harwell, UK.

YANASE, S., GOTO, N. & YAMAMOTO, K. 1988 Stability of dual solutions of the flow in a curved circular tube. *J. Phys. Soc. Japan* **57**, 2602–2604.

YANG, Z.-H. & KELLER, H. B. 1986 Multiple laminar flows through curved pipes. *Appl. Numer. Maths* **2**, 257–271.

YAO, L.-S. & BERGER, S. A. 1988 The three-dimensional boundary layer in the entry region of curved pipes with finite curvature ratio. *Phys. Fluids* **31**, 486–494.

YARBOROUGH, J. M. 1974 cw dye laser emission spanning the visible spectrum. *Appl. Phys. Lett.* **24**, 629–630.

YEE, G., CHILUKURI, R. & HUMPHREY, J. A. C. 1980 Developing flow and heat transfer in strongly curved ducts of rectangular cross section. *Trans. ASME* C: *J. Heat Transfer* **102**, 285–291.